

DESIGN OPTIMIZATION OF THE DOUBLE DELTA DOPING HEMT

by

Mincheol Lee

A thesis submitted to the Faculty of the University of Delaware in partial fulfillment of the requirements for the degree of Master of Science in Electrical and Computer Engineering

Summer 2018

© 2018 Mincheol Lee
All Rights Reserved

DESIGN OPTIMIZATION OF THE DOUBLE DELTA DOPING HEMT

by

Mincheol Lee

Approved: _____
Yuping Zeng, Ph.D.
Professor in charge of thesis on behalf of the Advisory Committee

Approved: _____
Kenneth E. Barner, Ph.D.
Chair of the Department of Electrical and Computer Engineering

Approved: _____
Babatunde A. Ogunnaike, Ph.D.
Dean of the College of Engineering

Approved: _____
Ann L. Ardis, Ph.D.
Senior Vice Provost for Graduate and Professional Education

ACKNOWLEDGMENTS

I would first like to express my gratitude to the South Korean Navy. Due to their incredible support for two years, I could broaden my insight and knowledge in electrical engineering.

I would also like to thank my thesis advisor, Dr. Zeng, and group members. I was able to build up my motivation and relevant knowledge during our many group meetings. I had to learn how to create simulations starting from nothing. It wasn't an easy task. Each simulation code and theory in this thesis represents every struggle and piece of knowledge I've gained over the past two years.

I thank my friends Kelli, Simone, and Anish. I am happy to have shared memories with them.

Thank you to my family and my love. You are the reason for my life.

TABLE OF CONTENTS

LIST OF TABLES	vi
LIST OF FIGURES	vii
ABSTRACT	ix

Chapter

1	INTRODUCTION : THE IMPORTANCE OF THE HEMT SIMULATION MODEL	1
2	THE ADVANTAGES OF THE HEMTS.....	3
2.1	The Advantages of the III-V Group Materials	3
2.1.1	The Electrical properties of III-V Group Materials.....	3
2.1.2	The Epitaxial Growth for the III-V Group Materials	6
2.2	The characteristics of the Field Effect Transistors	8
2.2.1	MOSFETs.....	8
2.2.1.1	Transit time.....	9
2.2.1.2	Cutoff-frequency	10
2.2.1.3	Limit of MOSFETs.....	11
2.2.2	MESFETs	12
2.2.2.1	The transconductance of the MESFETs	12
2.2.3	HEMTs	14
2.2.3.1	The characteristics of the HEMTs	15
2.2.3.2	The impact of delta doping layer on the HEMTs	16
2.2.4	The state of art of the HEMTs.....	18
3	THE SIMULATION SET-UP	20
3.1	The Sentaurus TCAD	20
3.1.1	The Simulation Tools	20
3.1.2	The Simulation Flows.....	21
3.2	Applied Physics models	23

3.2.1	The Fermi Dirac distribution	23
3.2.2	The interface of the semiconductor	26
3.2.2.1	The heterojunction.....	26
3.2.2.2	The Schottky junction.....	27
3.2.3	Carrier transport model.....	30
3.2.3.1	The carrier drift velocity.....	30
3.2.3.2	The carrier diffusion	31
3.2.3.3	The total current density	31
3.2.3.4	High-field saturation model.....	33
3.2.4	Recombination model.....	34
4	THE MODEL DESCRIPTION AND RESULTS	35
4.1	The Simulation Platform	35
4.2	Model Descriptions and Results	40
5	CONCLUSION	51
	REFERENCES	52
Appendix		
A	THE STRUCTURE CODES	55
B	THE SDEVICE CODES	70

LIST OF TABLES

Table 1: Electron mobility and effective mass of silicon and III-V group materials. [5]	4
--	---

LIST OF FIGURES

Figure 2.1: The low field mobilities of semiconductors. [4]	4
Figure 2.2: The drift-velocity of Electrons at high-field. [4]	5
Figure 2.3: The formation of strained pseudomorphic layer. [9]	7
Figure 2.4: The relationship between lattice parameter and Γ energy bandgap. [9]	7
Figure 2.5: The small circuit design of the MOSFETs. [14]	10
Figure 2.6: Schematic of the MESFETs.	12
Figure 2.7(a): The Schematic of the HEMTs.	15
Figure 2.7(b): The heterojunction energy band-diagram of the HEMTs.	15
Figure 2.8: The development of HEMTs cutoff-frequency over the past twenty years.	18
Figure 3.1: The simulation flow.	22
Figure 3.2: The Fermi-Dirac distribution. [6]	24
Figure 3.3: The energy-band diagram of isotype heterojunction.	26
Figure 3.4: The energy band-diagram of Schottky barrier. (a) is before contact, (b) is after contact. [6]	28
Figure 3.5: The energy band-diagram of Schottky barrier. (a) is when reverse bias is applied, (b) is when forward bias is applied. [6]	28
Figure 3.6: The tunneling behaviors (a) Before bias (b) After reverse bias. [17]	29
Figure 4.1: The Schematic of the InGaAs channel HEMT.	35
Figure 4.2: The schematic of the simulation structure.	36
Figure 4.3(a): The mesh size below the gate region	36
Figure 4.3(b): The I_D vs V_{GS} curve depending on mesh size.	37
Figure 4.3(c): The I_D vs V_{DS} curve depending on mesh size.	37
Figure 4.4(a): The comparison of I_D vs V_{GS} with simulation results and experiment data. ..	38

Figure 4.4(b): The comparison of I_D vs V_{DS} with simulation results and experiment data. ..	39
Figure 4.5(a): The comparison of I_D vs V_{GS} depending on carrier transport model.....	40
Figure 4.5(b): The comparison of I_D vs V_{DS} depending on carrier transport model.	41
Figure 4.6: The comparison of I_D vs V_{GS} depending on the cap doping concentration.	41
Figure 4.7: The I_D vs V_{GS} curves for various length of L_{side}	42
Figure 4.8: The I_D vs V_{GS} for various values of t_{ins}	43
Figure 4.9: I_D vs V_{GS} curves for various length of L_{gate}	44
Figure 4.10(a): I_D vs V_{GS} curves for HEMT with different Indium mole fraction.	45
Figure 4.10(b): I_D vs V_{DS} curves for HEMT with different Indium mole fraction.	45
Figure 4.11(a): The I_D vs V_{GS} curves for various values of $N_{\delta 1}$	46
Figure 4.11(b): The I_D vs V_{GS} curves for various values of $N_{\delta 2}$	47
Figure 4.12: The Schematic for buried S/D for HEMT.....	48
Figure 4.13(a): Comparison of simulation performance with normal S/D and buried S/D. .	49
Figure 4.13(b): Comparison of simulation performance with normal S/D and buried S/D. .	49

ABSTRACT

In this thesis, the DC performance of the high-electron mobility transistor (HEMT) on GaAs substrate is studied based on a Sentaurus TCAD simulation. Poisson's equation, carrier temperature, and carrier continuity equations are included in the hydrodynamic model, and higher order effects such as electron velocity saturation and velocity overshoot are considered. The impact of double delta-doping layers on device performances are discussed. Further optimization methods like buried source and drain structure and channel compositions are proposed. It shows that the Off-current is reduced by 50% at a low drain bias and the On-current is increased by 26% at a high drain voltage bias.

Chapter 1

INTRODUCTION : THE IMPORTANCE OF THE HEMT SIMULATION MODEL

In the microwave, millimeter wave, and Monolithic Microwave Integrated Circuit (MMIC) technology applications, the importance of High Electron Mobility Transistors (HEMTs) has been growing. The importance of HEMT's higher cutoff frequency due to enhanced electron movement in the Two-Dimensional-Electron-Gas (2DEG) region, low noise and operation in terahertz regime has influenced its popularity in the integrated circuit field.

Extensive research on HEMTs have been conducted in recent years. Most of them focused on the downscaling of litho-feature size, parasitic resistance/capacitance reduction [1]-[3]. They have also focused on structural optimization but have not presented simulation models using double-delta doping. This thesis builds on this research by creating a simulation model using double-delta doping to predict the performance and optimization of the device. The simulation model's accuracy is verified by comparing its results with current published data on HEMT.

In chapter 2, the advantages of HEMTs and III-V group materials are introduced. Through research, III-V group materials have been found to perform better than silicon due to their electrical properties and their ability to create heterojunctions. Chapter 3 introduces the TCAD simulation program and applied physics models. This chapter explains the reasoning for selecting featured physics models to describe the device's working principles. In chapter 4, after verifying the simulation model's accuracy by

comparing it with current published experimental data, model descriptions for the structural variables and results are covered. In conclusion, the buried source and drain HEMT simulation structure is redesigned for further performance of both Off-current and On-current.

Chapter 2

THE ADVANTAGES OF THE HEMTS

With the increasing needs for data usage and storage in millimeter wave devices, optical communication, medicine, and security, there has been a growing body of research on high-frequency devices over the years. To improve upon high-frequency devices, it is necessary to reduce gate lengths, transit time, and operation voltage for future military applications and satellites.

The excellent performance of HEMTs comes from its material and heterojunction. In this section, the advantages of III-V group materials and HEMTs will be introduced by comparing its characteristics with those of the other Field Effect Transistors (FETs) such as Metal Oxide Semiconductor Field Effect Transistors (MOSFETs) and Metal Semiconductor Field Effect Transistors (MESFETs).

2.1 The Advantages of the III-V Group Materials

To form a 2DEG region, a heterojunction interface is required. III-V group materials have different bandgap and can form a heterojunction interface. In the following section, the advantages of III-V group materials are explained, and their exceptional electrical properties are highlighted. Also, to form a heterojunction and delta-doped layer, the Molecular Beam Epitaxial (MBE) growth technique is used.

2.1.1 The Electrical properties of III-V Group Materials

The III-V group materials have several advantages over silicon, which is normally used for homojunction devices. Figure 2.1 shows the electron mobility of common semiconductors at low-field. III-V materials such as InSb, InAs, GaAs, GaSb,

and InP shows at least five times higher mobility than silicon. Besides, the electron mobility is higher at narrow bandgap materials due to decreased band interaction. [4]

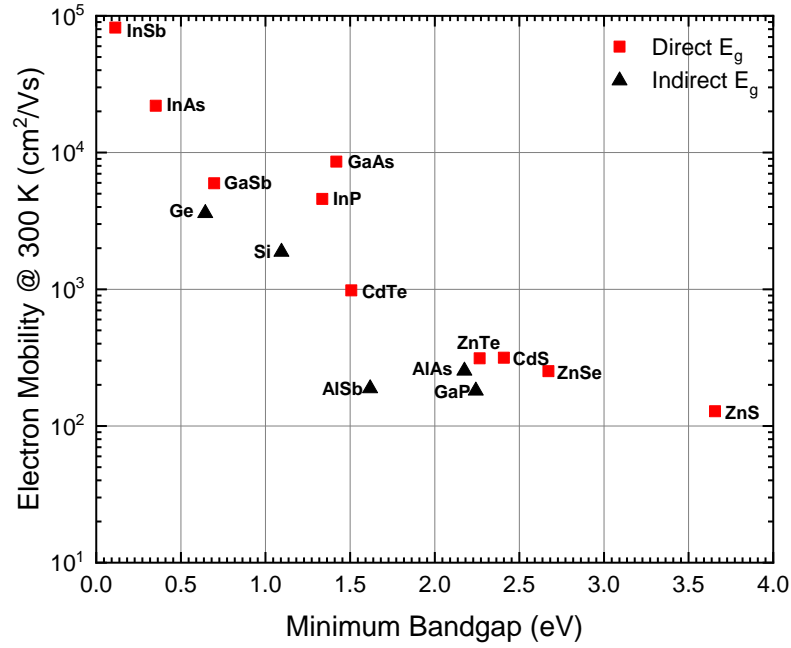


Figure 2.1: The low field mobilities of semiconductors. [4]

Table 2.1: Electron mobility and effective mass of silicon and III-V group materials. [5]

Material	m^*/m_0	$\mu_{300K} (cm^2/Vs)$	$\mu_{peak} (cm^2/Vs)$
Si	0.259	1750	500000 ($T \sim 8 K$)
GaAs	0.067	9340	400000 ($T = 28 - 40 K$)
GaSb	0.039	12040	12700 ($T = 77 K$)
InP	0.07927	6460	400000 ($T \sim 45 K$)
InAs	0.024	30000	170000 ($T = 77 K$)
InSb	0.013	77000	1100000 ($T \sim 50 K$)

The relationship between effective mass and carrier velocity can be found in Table 2.1. The III-V group materials show much lower effective mass and higher mobility than silicon. The lighter effective mass (m^*) of III-V group materials increases mobility and drift-velocity (v_d). The carrier mobility (μ) can be expressed by [4],[6]

$$\mu = \frac{v_d}{\mathcal{E}} = \frac{e\tau}{m^*}, \text{ where } v_d = \left(\frac{e\tau}{m^*}\right) \mathcal{E} \quad (2.1)$$

Where m^* is the effective mass, e is the charge, τ is the relaxation time, which is the term between collision, \mathcal{E} is the electric-field.

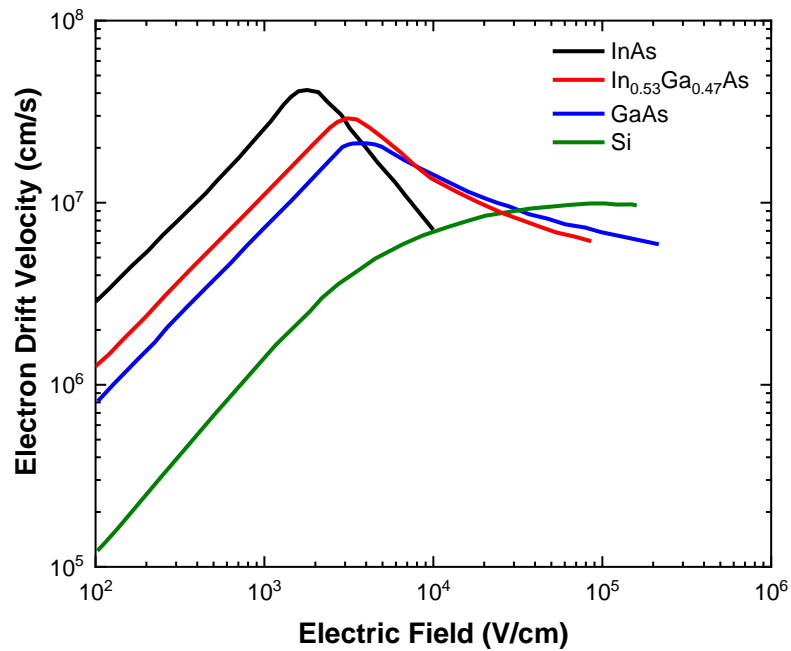


Figure 2.2: The drift-velocity of Electrons at high-field. [4]

At the high electric-field, the drift-velocity is drastically changed depending on the electric-field strength. Figure 2.2 shows the drift-velocity of electrons depending on

high electric field. The drift-velocity of III-V group material is much higher than silicon. The drift velocity increases proportionally with the electric-field. But at certain points, drift velocities are dropped because the carriers acquire higher energy and dispel its energy by acoustic phonons to the lattice. [4]

2.1.2 The Epitaxial Growth for the III-V Group Materials

The epitaxial growth means growing a different layer on top of the original substrate. Thus, an atomic lattice match should be considered to grow a heterostructure on the substrate. The lattice mismatch occurs when epitaxial layer and substrate lattice parameter is different. It causes a carrier transport degradation because of interface defects. Thus, the heterostructure growing techniques have been studied to solve the lattice mismatch. Earlier approaches used the pseudomorphic growth technique, and nowadays the metamorphic growth technique is used for HEMTs. [7], [8],[9]

The pseudomorphic growth technique allows for the growth of an epitaxial layer on top of a substrate when the lattice mismatch is small, and the epitaxial layer is thin. When an epitaxial layer is grown on top of target material, the epitaxial layer is strained to match the lattice. Figure 2.3 shows the formation of a strained pseudomorphic layer. Figure 2.4 represents the relationship between lattice parameter and Γ energy bandgap of InAs, GaAs, and AlAs. [9] Thus, depending on compound material's mole fractions for example $\text{In}_{(x)}\text{Al}_{(1-x)}\text{As}$, the lattice parameter changes, a lattice match should be considered for flawless interface.

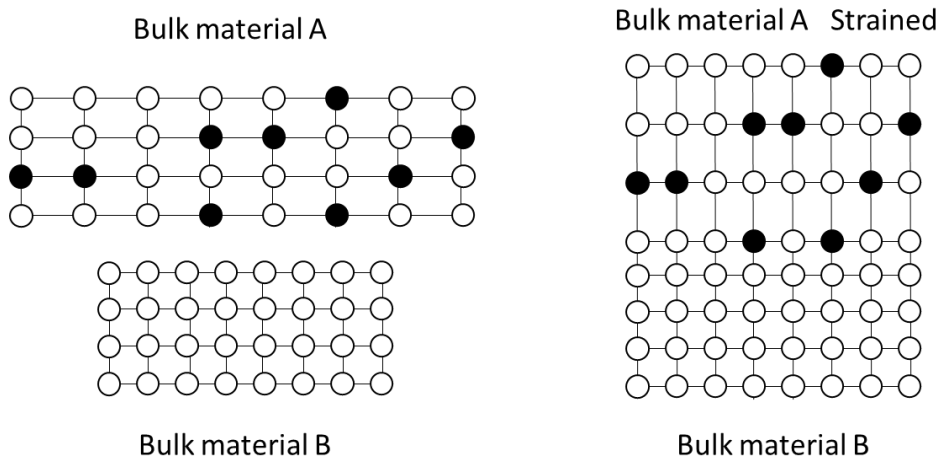


Figure 2.3: The formation of the strained pseudomorphic layer. [9]

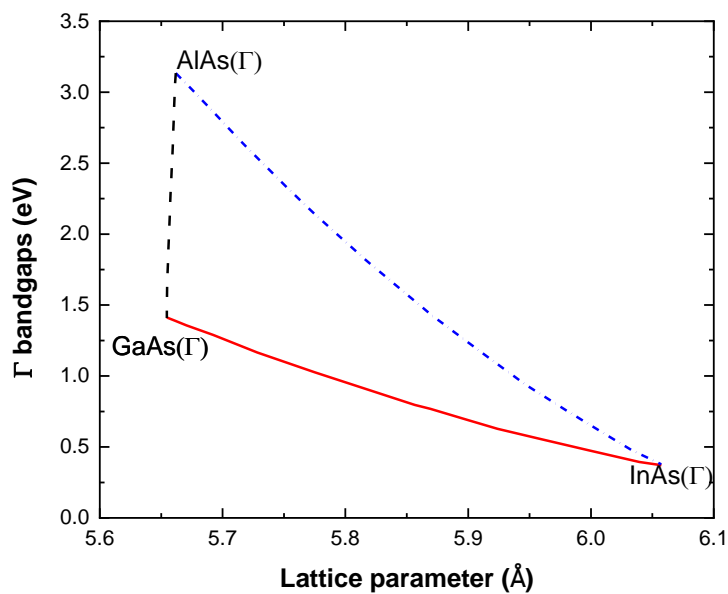


Figure 2.4: The relationship between lattice parameter and Γ energy bandgap. [9]

The metamorphic growth technique introduces a linearly graded buffer layer between channel and substrate to reduce dislocation density. The advantage of the metamorphic growth technique is the control of mole fractions in channel materials for improved performance. While the pseudomorphic technique is useful for the only lattice matched compound materials. For example, the indium concentration can be adjusted by introducing a graded InAlAs buffer between InGaAs channel and GaAs substrate. [7], [8]

The MBE process commonly is used for both the pseudomorphic and metamorphic growth technique. This MBE process provides several advantages for III-V compound semiconductors such as growing high purity thin layers due to ultra-high-vapor pressure, an abrupt structure for heterointerface, and the profiles of impurities concentrations. [10] This is advantageous for making heterojunctions, such as AlGaAs/GaAs on AlGaAs substrate, InAlAs/InGaAs on GaAs or InP substrates. In addition, the delta-doped layer can be confined at the selective location.

2.2 The characteristics of the Field Effect Transistors

The following section, the advantages and disadvantages of MOSFETs, MESFETs, and HEMTs are explained by comparing the transconductance. This transconductance can be calculated from the simulation results of the current that are presented in this thesis.

2.2.1 MOSFETs

The silicon-based application, MOSFETs, have dominated the VLSI technology fields. The MOSFET's advantages come from the substrate material, silicon. The advantages of silicon are its abundance, chemical stability, and silicon surface can be

oxidized with high-quality oxide, SiO₂. [4] But, the MOSFETs have its limit for high-speed performance of a circuit. It can be presented with the transit time (τ_t) and cutoff-frequency (f_T).

2.2.1.1 Transit time

Transit time represents the time which is required to move carriers from source to drain. The transit time (τ_t) of MOSFET can be expressed by [11],[12]

$$\tau_t = \frac{L}{v} \quad (2.2)$$

Where L is the length of the channel, v is the velocity of the carrier.

In the MOSFET, drift velocity governs the transit mechanism. Drift velocity (v_d) can be expressed with mobility (μ_n) and electric-field (\mathcal{E}). It is given by [6],[11]

$$v_d = \mu_n \times \mathcal{E} \quad (2.3)$$

The average electric-field in MOSFET can be calculated by the voltage across the channel which is divided by channel length. Then, the drift velocity is defined by

$$v_d = \mu_n \times \mathcal{E} = \mu_n \times \left(\frac{V_{GS} - V_{TH}}{L} \right) \quad (2.4)$$

Where V_{GS} is the gate to source voltage, V_{TH} is threshold voltage.

Also, it can be expressed by

$$\tau_t = \frac{L}{v} = \frac{L^2}{\mu_n(V_{GS} - V_{TH})} \quad (2.5)$$

Thus, increased mobility and the reduced channel length is required for reducing transit time.

2.2.1.2 Cutoff-frequency

The cutoff-frequency is the important parameter, which can express a device's performance at high-frequency. [13] Figure 2.5 shows the small-signal circuit of MOSFET. [14] When the output is short-circuited, capacitances (C_{GS} and C_{GD}) are parallel. Thus, input and output current can be expressed by [14]

$$\begin{aligned} \text{(input current) } i_g &= j2\pi f(C_{GS} + C_{GD})v_{gs} \\ &\approx j2\pi f(C'_{OX}WL)v_{gs} \end{aligned} \quad (2.6)$$

$$\text{(output current) } i_d = g_m v_{gs} \quad (2.7)$$

Where $C_{GS} + C_{GD} \approx C'_{OX}WL$, and $i_d = i_g$ (current gain drops to unity).

Thus, by definition, cutoff-frequency is expressed by [14]

$$f_T = \frac{g_m}{2\pi C'_{OX}WL} \text{ or } \omega_T = 2\pi f_T = \frac{g_m}{C_{gate}} \quad (2.8)$$

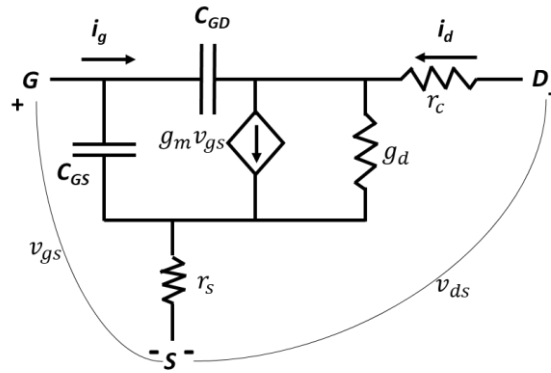


Figure 2.5: The small circuit design of the MOSFETs. [14]

The transconductance (g_m) in equation (2.8) can be calculated from the MOSFET saturation current. In MOSFET, the saturation current (I_D) is given by [6]

$$I_{DSat} = \frac{\mu_n C_{ox} W}{2L} (V_{GS} - V_{TH})^2 \quad (2.9)$$

Where C_{ox} is oxide capacitance, W is the width of the gate.

The transconductance can be calculated by [6]

$$g_m = \frac{\partial I_D}{\partial V_{GS}} = \frac{\mu_n C_{ox} W}{L} (V_{GS} - V_{TH}) \quad (2.10)$$

In summary, to improve transit time and cutoff-frequency, it is required to reduce gate capacitance (C_{gate}), the channel length (L), and increase transconductance (g_m), mobility (μ_n).

2.2.1.3 Limit of MOSFETs

There are challenges to modify the above-mentioned factors in MOSFETs. For the increased capacitance (C_{gate}), the gate should be close to the channel. This is possible by decreasing oxide thickness with high k materials like Hafnium oxide, but as Equivalent Oxide Thickness (EOT) is shorter, mobility degradation happens.

As channel length (L) becomes close to the depletion region length, some detrimental physical phenomena, such as drain induced barrier lowering (DIBL), surface scattering, velocity saturation, impact ionization, and hot electrons occur.

Regarding mobility, the III-V group materials show higher mobility. For example, the carrier mobility of GaAs is five times higher than that of silicon. However, making III-V MOSFETs using its higher mobility is a tough task because it is difficult to grow native oxide for GaAs substrate. Besides, GaAs has high interface density which results in improper CV characteristics and low transconductance. [15]

2.2.2 MESFETs

In MOSFETs, it is required to reduce channel length (L) for higher transconductance and cutoff-frequency. The tradeoff is improved transconductance by reducing channel length (L) and increased threshold voltage results from being increased doping level. Therefore, reducing an oxide thickness is necessary for lowering the threshold voltage. In this respect, the MESFET structure has advantages because of a lack of an oxide layer below the gate. Also, MESFETs have material and structural advantages over MOSFETs. MESFETs use III-V group materials which have higher electron velocity and mobility. In addition, GaAs semi-insulating layer provides smaller parasitic resistance. Thus, MESFET shows smaller transit time and higher cutoff frequency than MOSFETs. [15],[16]

2.2.2.1 The transconductance of the MESFETs

Figure 2.6 shows the schematic of the MESFETs.

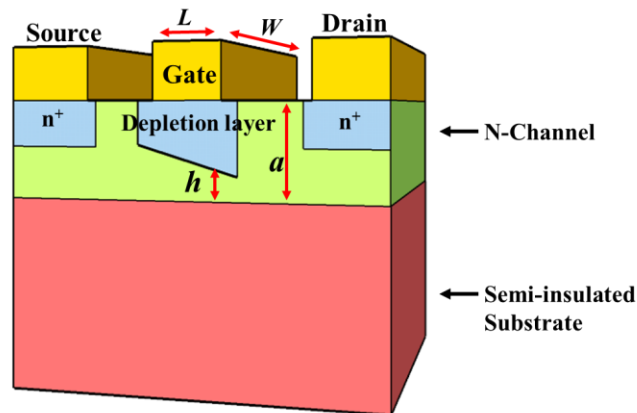


Figure 2.6: Schematic of the MESFETs.

The current characteristic can be defined by Ohm's law due to an Ohmic contact in source and drain region. The current of MESFET is given by [15],[17]

$$dV = I_{ds} \times dR = \frac{I_{ds} dx}{q\mu_n N_D W (a - h)} \quad (2.11)$$

Where a is channel thickness, h is the depletion layer thickness, L is the channel length, W is the channel width, q is the electronic charge, A is the conduction area. N_D is the donor concentration, I_{ds} is the channel current.

Then, Schottky barrier gate is considered between a source and drain to control the channel conductivity by changing a thickness of the conduction channel. The thickness of depletion layer (h) depends on the potential across the gate. It is given by [15],[17]

$$V(x) + V_{bi} - V_G = \frac{qN_D h^2}{2\epsilon} \quad (2.12)$$

Where V_G is the gate potential, V_{bi} is the built-in potential, $V(x)$ is the potential of the neutral channel.

The equation (2.12) can be express by [15],[17]

$$h = \sqrt{\frac{2\epsilon[V(x) + V_{bi} - V_G]}{qN_D}} \quad (2.13)$$

The channel thickness (a) can be defined by pinch-off voltage (V_{po}) which means the channel is fully depleted and the current is zero. It is given by [15],[17]

$$V_{po} = \frac{qN_D a^2}{2\epsilon} \quad (2.14)$$

Thus, the equation (2.11), (2.13) and (2.14) can be simplified by [15],[17]

$$I_D = g_0 \left\{ V_D - \frac{2 \left[(V_D + V_{bi} - V_G)^{3/2} - (V_{bi} - V_G)^{3/2} \right]}{3V_{po}^{1/2}} \right\} \quad (15)$$

where $g_o = \frac{q\mu_n N_D W a}{L}$

with the saturation voltage, $V_{Dsat} = V_{po} - V_{bi} + V_G$, the equation (2.15) can be expressed by [15],[17]

$$I_{Dsat} = \frac{q\mu_n N_D W a}{L} \left\{ \frac{V_{po}}{3} - \frac{2(V_{bi} - V_{GS})^{3/2}}{3V_{po}^{1/2}} - V_{bi} + V_{GS} \right\} \quad (2.16)$$

Using equation (2.16), the transconductance in linear region is given by [15],[17]

$$g_m = \frac{\partial I}{\partial V_G} | V_D = const \quad (2.17)$$

$$g_m = g_o \frac{(V_D + V_{bi} - V_G)^{1/2} - (V_{bi} - V_G)^{1/2}}{V_{po}^{1/2}} \quad (2.18)$$

With the saturation voltage and equation (2.17), the transconductance in saturation region can be express by [15],[17]

$$g_{m,sat} = \frac{q\mu_n N_D W a}{L} \left[1 - \left(\frac{V_{bi} - V_G}{V_{po}} \right)^{1/2} \right] \quad (2.19)$$

Thus, in MESFETs to get higher saturation current (I_{Dsat}) and transconductance (g_m), it is necessary to increase electron mobility (μ_n), doping concentration (N_D) and decrease channel length (L).

2.2.3 HEMTs

As mentioned in the earlier section, in order to reduce the device size, epitaxial layer thickness should be reduced while increasing doping concentration. However, increased doping level degrades electronic properties of channel region such as ionized impurity scattering and mobility reduction. The advantages of HEMTs comes from its discontinuity of bandgap. The discontinuity bandgap provides a 2DEG region, which allows electrons to be separated from impurities.

2.2.3.1 The characteristics of the HEMTs

Figure 2.7(a) presents the schematic design of HEMT. The source and drain are contacted with the heavily n-doped cap layer to form an ohmic contact. The gate is a Schottky contact with the wide-bandgap material. The HEMTs layers consist of a wide-bandgap material which is a selectively doped, a spacer layer, a buffer layer, and a substrate, as well as a narrow bandgap consisting of a channel layer.

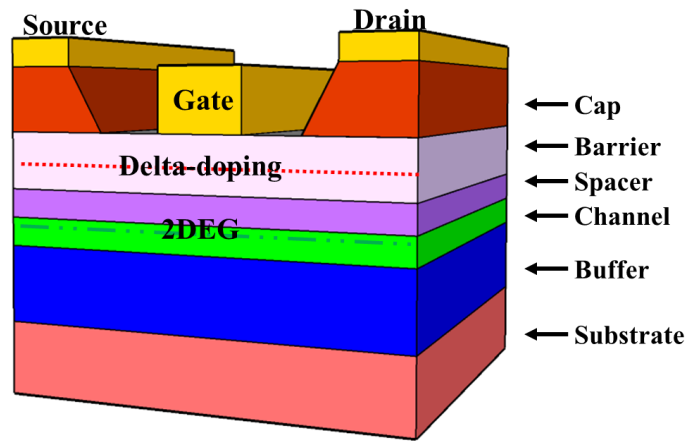


Figure 2.7(a): The Schematic of the HEMTs.

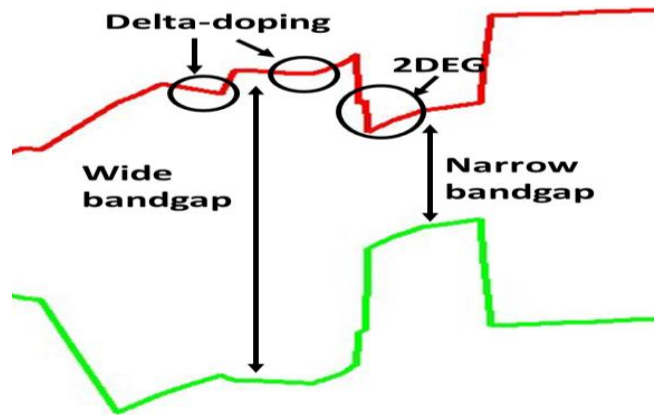


Figure 2.7(b): The heterojunction energy band-diagram of the HEMTs.

Figure 2.7(b) shows the heterojunction energy band diagram of the HEMTs. The performance advantages of HEMTs over MESFETs come from its heterojunction. When two different material's bandgaps are aligned by electron affinity rule, the electrons from wide-bandgap transport into the narrow-bandgap to occupy lower energy states. The ionized electrons are confined at the heterojunction interface because of the potential barrier. In this 2DEG region, electrons are accumulated without impurities. The advantage of 2DEG is the separation of electrons from the donor impurity atoms. In figure 2.7(b), The donor impurities exist on delta-doping location. Thus, the electrons mobility is enhanced because of reduced carrier scattering which comes from the heavily doped-layer. [18],[19] Besides, in 2DEG region, there are multiple discrete energy states. By filling up the lowest energy level, inter sub-band-scattering occurs at the next energy level. [19] Thus, depending on the field strength, HEMT shows different mobility characteristics. In the low field, ionized impurity scattering occurs. It can be prevented by the increasing of the spacer layer height. But it has detrimental effects on device such as reduced transferred electrons into the 2DEG and reduced transconductance (g_m). In high field, saturation velocity governs the device performance rather than impurity scattering. [15],[18], [19]

2.2.3.2 The impact of delta doping layer on the HEMTs

Earlier HEMTs designs consists of a heavily doped n+ AlGaAs which provides electrons, undoped AlGaAs which enhances the electron mobility further, undoped GaAs channel layer and a substrate. [15] With development of the epitaxial growth technique, such as MBE, selective doping, delta-doping is available instead of an entirely doped wide-bandgap layer.

Delta-doping allows for extremely reducing the size of dopant distribution to confine the dopant at the thin layer. Growing a delta-doped layer has several advantages over the introduction of an entire n-doped wide-bandgap layer. The delta-doped layer provides the highest electron density, mobility, and reduced short-channel effects. Thus, delta-doped HEMTs presents higher intrinsic transconductance by adjusting the gate to channel distance and convenience of changing threshold voltage by controlling the delta-doping concentration. [18]

With the equation for delta-doped GaAs FET, the relationship between the delta-doped layer and the maximum intrinsic transconductance on transistor can be analyzed. it is given by [18]

$$g_m = \frac{1}{L_g} (q\mu W_g n_{2DEG}) \left[1 + \left(\frac{q\mu n_{2DEG} d}{\varepsilon v_s L_g} \right)^2 \right]^{-1/2} \quad (2.20)$$

$$n_{2DEG} = N_D^{2D} - \frac{\varepsilon}{qd} \phi_B \quad (2.21)$$

This equation can be modified at the short channel, L_g goes to zero [18]

$$g_m = \frac{\varepsilon v_s W_g}{d} \quad (2.22)$$

Where n_{2DEG} is carrier concentration of the 2DEG, v_s is saturation velocity, d is the distance between delta-doped layer and gate, N_D^{2D} is the delta doping total density, ϕ_B is the Schottky barrier height, ε is the permittivity, q is the charge, L_g is channel length, W_g is gate width, μ is the mobility.

Thus, the distance d should be minimized to get the higher intrinsic transconductance. Self-aligned and gate-recess technique are widely used in recent HEMT structures for decreasing the gate to channel distance and suppress the short channel effect. [20],[21]

Also, higher doping concentrations, shorter gate length, and higher mobility are required for improving the transconductance.

The double delta-doped layer for increasing the transconductance has been reported. The impact of double doping layers is a reduction of parasitic resistance and increase of carrier density on a channel. Thus, the total current is increased, and access resistance is decreased. [21],[22]

2.2.4 The state of art of the HEMTs

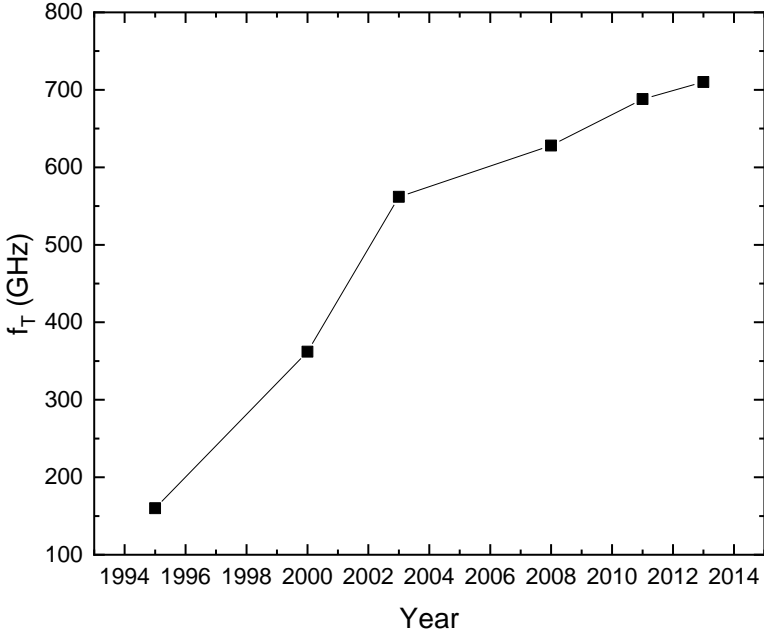


Figure 2.8: The development of HEMTs cutoff-frequency over the past twenty years.

HEMTs technology has been developed to achieve high-frequency performance since the 1980's. Figure 2.8 shows the development of HEMTs cutoff-frequency over the past twenty years. It shows the increase of cutoff-frequency based on research. [1],[20],[21],[23],[24],[25]

Earlier HEMT structures used AlGaAs/GaAs heterojunction bandgap. Nowadays InAlAs/InGaAs heterostructure is used because of its high mobility. Besides, high indium concentration channel metamorphic HEMTs (mHEMTs) are widely used with the development of an epitaxial growth technique. The substrate types are InP or GaAs, which are both widely studied. The InP based HEMT shows the highest record, but GaAs based HEMTs are also studied because of the advantages of GaAs substrate, including its cost and its larger dimension.

The highest on record cutoff-frequency is 710 GHz. This metamorphic HEMT uses the In_{0.7}Ga_{0.3}As/InAs/In_{0.7}Ga_{0.3}As 5 nm composite channel on InP substrate, and its gate length is 60 nm. [20]

In this thesis, cutoff-frequency 688 GHz model is used for the simulation. This device uses the smaller gate length, 40 nm, double-delta doped-layers, and In_{0.7}Ga_{0.3}As 10 nm channel on GaAs substrate. [21] Because this device has a much smaller gate length and double delta-doped layers, this is a good model for study of short-channel effect and other performances.

Chapter 3

THE SIMULATION SET-UP

3.1 The Sentaurus TCAD

The Sentaurus TCAD simulator provides an interface that can conduct 2D as well as 3D simulation of semiconductor and optoelectronic devices such as memory, transistors etc. Besides, TCAD analytical tools are used for checking device internal properties such as doping concentration, electric field, bandgap, a density of carrier, temperature and current density. It is useful for predicting device performance and additional modifications including material change. Thus, it is possible to save manufacturing cost and time using TCAD.

3.1.1 The Simulation Tools

The TCAD program consists of five types of simulator interfaces, which are a framework, process simulation, device creation and device simulation. This thesis uses Sentaurus Work Bench (SWB), Sentaurus Device Editor (SDE), Sentaurus Device (SDevice), Sentaurus Visual (SVisual) and Inspect tool.

The SWB is an interface tool for integration of TCAD software. It can visualize the third-party tools such as SDE, SVisual, SDevice and Inspect tool. All material files and parameter files which are produced at the third-party tools are shared in this framework interface. The SDE tool provides the interface for building two-dimensional or three-dimensional structures such as CMOS, FinFET, heterojunction devices, Memory devices, Nanowire devices, Optoelectronic devices, sensors and solar cell with Graphic User Interface (GUI) and command script. Additional functions such as defining contact region, adapting doping profiles and mesh can be added for a sophisticated simulation after generating the structure. [26]

The SDevice simulates the carrier transport in the defined structure. In electrode section, device's virtual terminal is set, and external voltage is applied to the device. The SDevice physical model contains conduction mechanisms such as traps, tunneling, and mobility models. Various electrical behavior models are applied at the device's grid point, which describes the device characteristics such as doping condition and material properties to approximate real device performance. [26]

The SVisual visualized electrical behavior such as Electric-field, Current-density, Bandgap, Doping-concentration, Mobility, Carrier temperature and Recombination rate with GUI for better understanding of semiconductor. In addition, it provides measurement tools such as a ruler and probe for checking electrical behavior at certain points. [26]

The INSPECT provides plots which is extracted from the simulation. The plots include important parameters such as I-V curves, maximum frequency, cut-off frequency, transconductance, and subthreshold swings for the analysis of device performance. [26]

3.1.2 The Simulation Flows

Figure 3.1 shows the flow of simulation. A new project can be generated at the SWB. Thereafter a new structure with GUI or command script at the SDE can be built. Materials parameter values are loaded at the parameter files. The material parameter file's value is normally set based on bulk material value. It can be adjusted manually with a calculated or experimented value. The external bias is applied at the contact point. To consider a convergence error, the contact metal should be removed from the SDE. The Appendix A includes codes for removing the metal parts. The contact metal part's electrical properties can be adjusted in SDevice which is included in the Appendix

B. The simulation structure after removing contact metal can be check in Figure 4.2 and Figure 4.3(a).

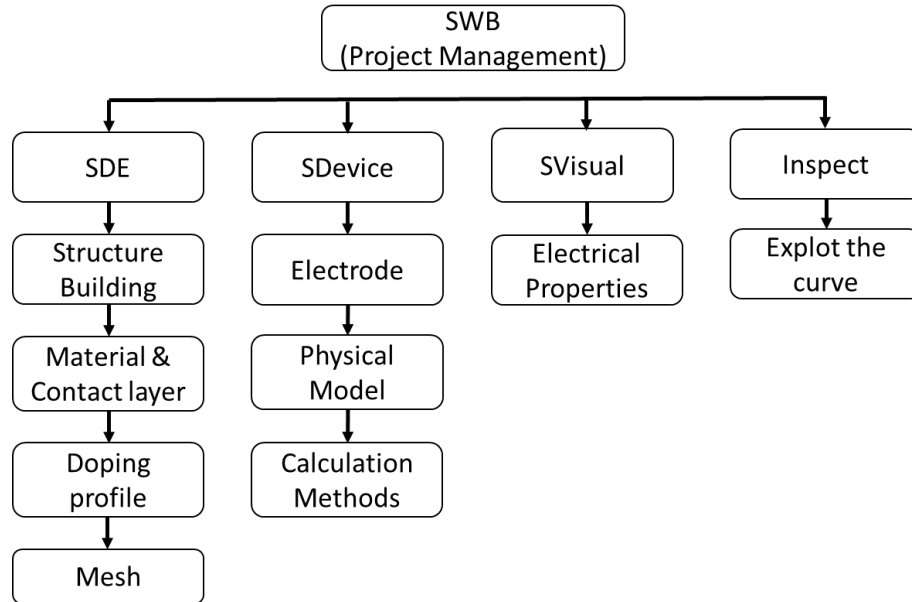


Figure 3.1: The simulation flow.

The next crucial step in the simulation’s calculation is making the grids points, also called the meshing process. The mesh describes materials characteristics. Newton’s iteration, a numeric analysis is basic operation principle to approximate the unknown value. The Poisson’s equations, current continuity equation, and additional equations are discretized at each mesh point. Thus, dense mesh assures the performance accuracy of prediction. The trade-off of having a smaller mesh size is higher accuracy but longer calculation time. [26] This is discussed in chapter 4.

The virtual terminal is defined at the SDevice. The ohmic contact or Schottky contact can be designated, and these contact definitions work as boundary conditions of

Newton's iteration. Physical models can be chosen depending on carrier transport models such as the Drift-Diffusion model, the Thermo-dynamic model, and the Hydro-dynamic model. The basic model is the Drift-diffusion model which contains Poisson's equations and carrier continuity equations. Also, the thermo-dynamic model includes self-heating equations, and the Hydro-dynamic model describes the carrier Energy or temperature distribution. [26],[27]. Then, calculation methods such as minimum/maximum step size, iteration number and error are set at the solve section of SDevice. After calculation, extracted graph curves can be checked at the Svisual and Inspect tool.

3.2 Applied Physics models

3.2.1 The Fermi Dirac distribution

The intensity of conductivity is determined by an energy bandgap. Every semiconductor material has an indigenous bandgap (E_g). The bandgap (E_g) is the distance between a conduction band (E_C) and a valence band (E_V). The conduction band (E_C) allows electrons to occupy empty available energy states. The valence band (E_V) is nearly in a full state. When an electric field is applied, electrons acquire enough energy to move to higher energy states. The Fermi energy level (E_f) is an important parameter to decide p- or n-type material. Because it means there is a fifty percent of probability in which the energy states that can be occupied by electrons. Thus, the Fermi energy level (E_f) is close to the conduction band (E_C), the material characteristic becomes n-type material.

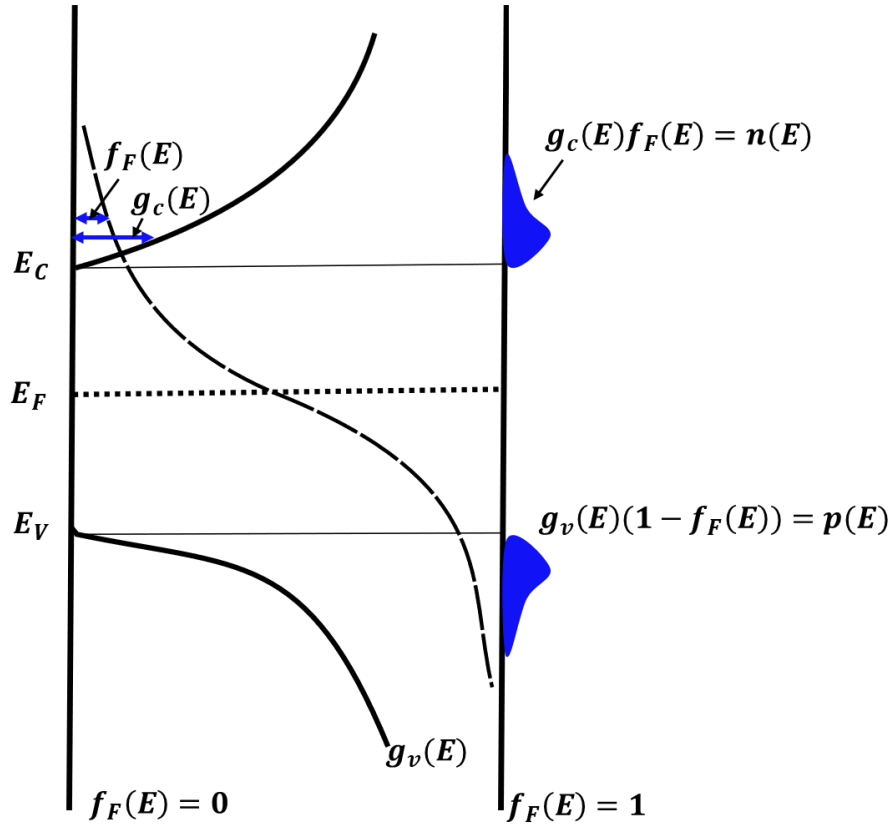


Figure 3.2: The Fermi-Dirac distribution. [6]

Figure 3.2 shows the number of electron concentration ($n(E)$) depending on density of energy states ($g_c(E)$) and Fermi Dirac distribution ($f_F(E)$).

The number of carriers, carrier concentration, can be calculated by the density of the quantum states and Fermi-Dirac probability function. The density of the energy states refers to the available energy states that can be occupied by electrons, and Fermi-Dirac probability ($f_F(E)$) means the probability of occupation by electrons. Thus, the concentration of carrier can be calculated using the above-mentioned factors. It is given by [6]

$$n_0 = \int g_c(E) f_F(E) dE, \quad p_0 = \int g_v(E) [1 - f_F(E)] dE \quad (3.1)$$

Where n_0, p_0 is the concentration of electron and the hole respectively, $g_c(E), g_v(E)$ are the density of energy states of the conduction band and valence band respectively.

The Boltzmann approximation (3.2) and $g_c(E)$ (3.3) are given by [6]

$$f_F(E) = \frac{1}{1 + \exp\left(\frac{E - E_F}{kT}\right)} \approx \exp\left[\frac{-(E - E_F)}{kT}\right] \quad (3.2)$$

$$g_c(E) = \frac{4\pi(2m_n^*)^{3/2}}{h^3} \sqrt{E - E_c} \quad (3.3)$$

The electron concentration can be calculated by [6]

$$n_0 = \int_{E_c}^{\infty} \frac{4\pi(2m_n^*)^{3/2}}{h^3} \sqrt{E - E_c} \exp\left[\frac{-(E - E_F)}{kT}\right] dE \quad (3.4)$$

It can be simplified by [6]

$$n_0 = 2 \left(\frac{2\pi m_n^* kT}{h^2}\right)^{3/2} \exp\left[\frac{-(E_c - E_F)}{kT}\right] \quad (3.5)$$

Where m_n^* is the effective mass of the electron, h is the Planck's constant, kT it the thermal voltage.

Thus, by the equation, the number of electrons or holes can be adjusted by the location of the Fermi energy level (E_f). The way of the changing the location of the Fermi level is the doping process.

The TCAD simulation basically uses Boltzmann probability approximation to calculate the total number of the carrier. [26] But this approximation is not suitable for a heavily doped model. This thesis's model uses heavily doped contact layers and delta-doped layers. Both electron concentrations are higher than 10^{19}cm^{-3} . Thus, activation

of the Fermi-Dirac distribution function in the TCAD is required instead of the Boltzmann approximation for exact calculation of the carrier.

3.2.2 The interface of the semiconductor

There are two types of interface junctions- semiconductor to semiconductor junction and the metal to semiconductor junction.

3.2.2.1 The heterojunction

The important characteristic of the heterojunction between semiconductors is its energy bandgap discontinuity. If two different energy-bandgap materials use the same types of impurities, this is called isotype heterojunction. When the two different energy-bandgap materials use different types of impurities, it is called anisotype heterojunction.

[6] Figure 3.3 shows the energy-band diagram of isotype heterojunction. [6]

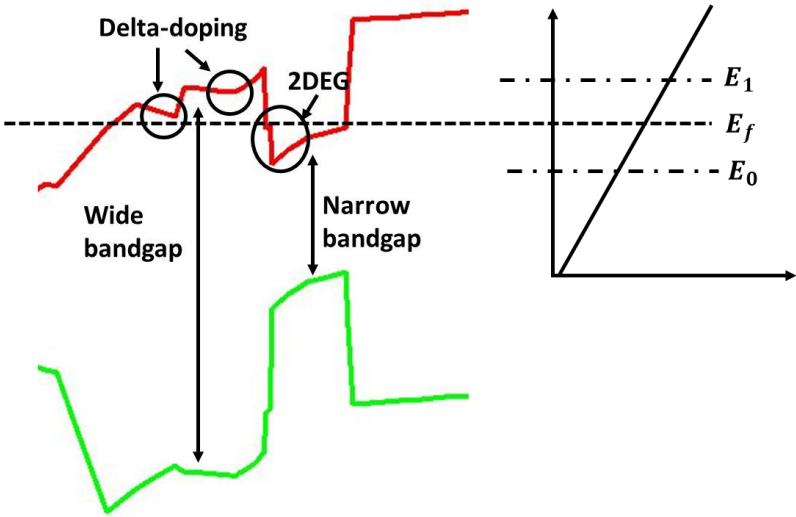


Figure 3.3: The energy-band diagram of isotype heterojunction.

In the same vacuum level, the larger energy-bandgap and narrow energy bandgap are aligned with discontinuity region. The advantage of energy-band dislocation is the 2-Dimensional Electron Gas (2DEG) potential well. When energy-bandgaps are aligned, the electrons of wide energy-bandgap flow to the potential well. The electrons are quantized at the 2DEG region and show improved mobility because there is a lack of scattering of the impurities. [6]

InAlAs / InGaAs heterostructure shows excellent performance because of a larger conduction band dislocation which can make the deeper 2DEG region and improved electron mobility in InGaAs channel. [28] In this simulation, to make heterojunction interface, 2 nm & 6nm In_{0.52}Al_{0.48}As barrier, 2 nm In_{0.52}Al_{0.48}As spacer layer, 1 nm In_{0.7}Al_{0.3}As spacer, and 10 nm In_{0.7}Ga_{0.3}As channel is used.

3.2.2.2 The Schottky junction

The way to contact metal to a semiconductor is the Schottky junction. It allows the current to flow in one polar direction. Figure 3.4(a)(b) show energy-band diagram of Schottky contact. In an n-type semiconductor, when metal work-function (ϕ_m) is larger than n-type semiconductor work-function (ϕ_s), the Schottky barrier height (ϕ_B) is formed due to energy bandgap alignment. This initial barrier height ($\phi_B = \phi_m - \chi$) is defined by the different level of the metal work-function (ϕ_m) and electron affinity (χ). It remains constant and, block or allow the current depending on applied bias. [6] In reverse bias, a negative bias is applied to the metal, the semiconductor to metal barrier height is increased to $e(V_{bi} + V_R)$ in Figure 3.5(a). In forward bias, a positive bias is applied to metal, the semiconductor to metal barrier height is decreased to $e(V_{bi} - V_a)$ in Figure 3.5(b). [6] Where V_{bi} is the built-potential ($\phi_B - \phi_n$), V_R is the reverse bias, V_a is the forward bias.

Thus, only forward bias allows the current to flow while blocking the current under reverse bias.

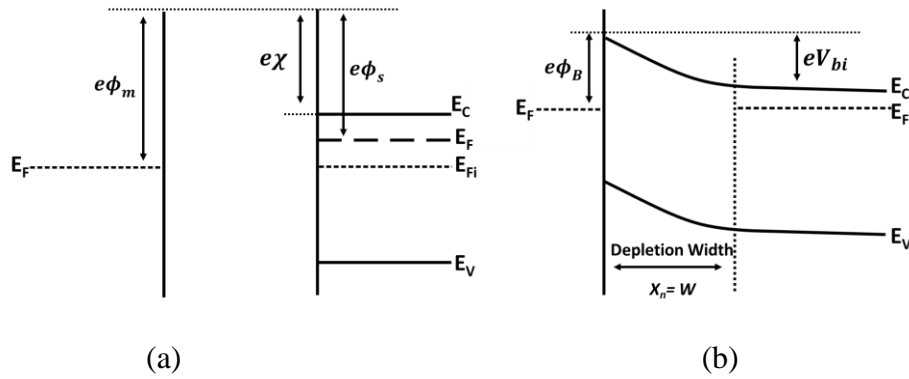


Figure 3.4: The energy band-diagram of the Schottky barrier. (a) is before contact, (b) is after contact. [6]

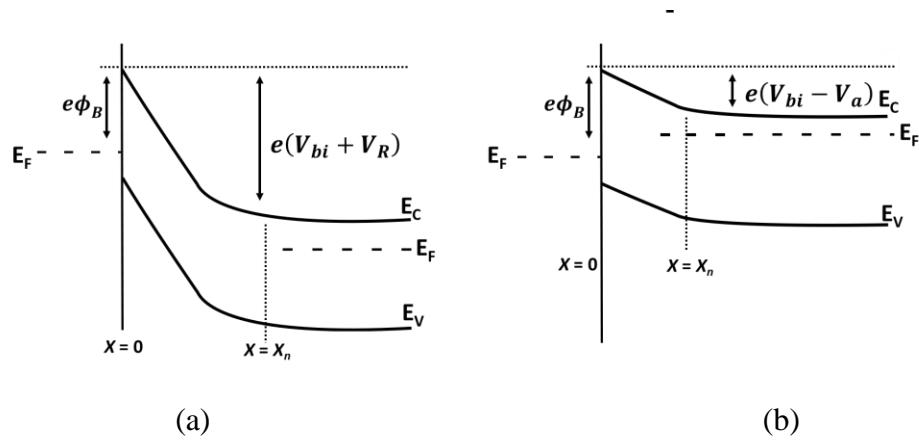


Figure 3.5: The energy band-diagram of the Schottky barrier. (a) is when the reverse bias is applied, (b) is when the forward bias is applied. [6]

The Schottky junction can work as an ohmic contact. When reducing the depletion width, the electrons can tunnel the Schottky barrier. The depletion width is given by [6]

$$W = x_n = \left[\frac{2\epsilon_s(V_{bi} + V_R)}{eN_d} \right]^{1/2} \quad (3.6)$$

Where ϵ_s is semiconductor permittivity, N_d is the doping concentration.

Thus, when doping concentration is increased, the depletion width decreases.

Figure 3.6 shows the tunneling behavior under a heavily doped condition. Because the barrier width is thin, electrons can tunnel the Schottky barrier.

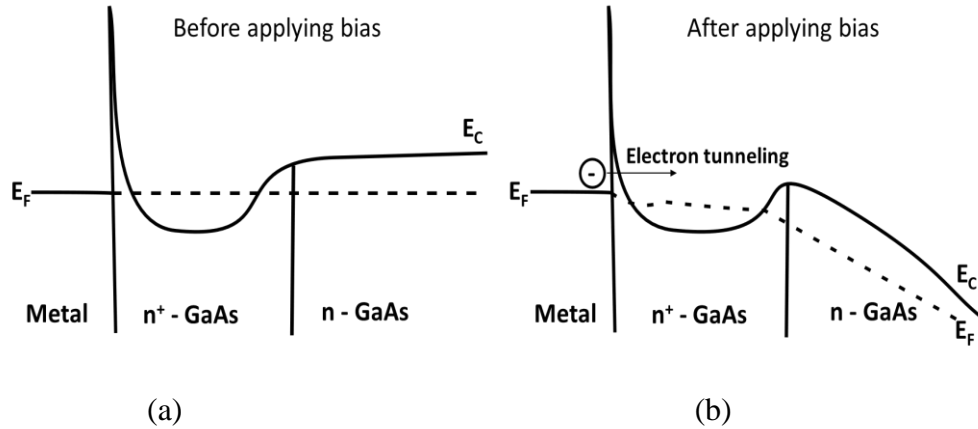


Figure 3.6: The tunneling behaviors (a) Before bias (b) After reverse bias. [17]

The minimum contact resistance of this heavily doped Schottky barrier contact is given by [17]

$$r_{c,min} = \frac{(2\pi mkT)^{1/2}}{q^2 N_d} \quad (3.7)$$

Where m is effective electron mass.

Thus, with increased doping concentration, tunneling is possible in both directions, and the minimum contact resistance is lowered working as an ohmic contact.

A lot of studies have reported the reduction of a source and drain contact resistance. The low resistive resistance is available with contacting a non-alloyed metal with a highly conductive n-doped semiconductor layer. The advantages of non-alloyed metal are its smooth morphology and uniformity of contact surface.[29] In a simulation, Non-alloyed or alloyed metal can be set by work-function value. The contact material's work-function is automatically set at the SDE depending on the material part, but it can be adjusted manually by inputting a specific number at the electrode section. This thesis uses the S/D ohmic contact and resistance is $100 \Omega/\mu\text{m}$.

3.2.3 Carrier transport model

It is very important to choose a suitable carrier transport model for the device simulation. In this section, the Hydrodynamic model is introduced for the HEMT simulation.

3.2.3.1 The carrier drift velocity

As stated in chapter 2, the free carriers- the electrons and holes, which have random thermal motions are accelerated as electric-field (\mathcal{E}) is increased and get additional drift velocity. Thus, total drift current by electrons and holes can be given by [6]

$$J_{drift} = e(\mu_n n + \mu_p p)\mathcal{E} \quad (3.8)$$

Where e is the magnitude of electronic charge, n and p are electrons and holes concentration respectively.

3.2.3.2 The carrier diffusion

When carriers are diffused from higher density into lower density, there are diffusion currents. It is given by [6]

$$\text{for electrons, } J_{nx,dif} = eD_n \frac{dn}{dx}, \quad (3.9)$$

$$\text{for holes, } J_{px,dif} = -eD_p \frac{dp}{dx} \quad (3.10)$$

where D_n, D_p are electrons and holes diffusion coefficient, respectively.

3.2.3.3 The total current density

The total current density is obtained by adding up the above-mentioned drift current and diffusion current. This total current density is used for the carrier continuity equation.

In the TCAD simulation, carrier continuity equation is applied to the mesh points to tract the current flux, generation rate, and recombination rate at each location and time. It is given by [26]

$$\text{for electrons, } \frac{\partial n}{\partial t} = \frac{1}{q} \frac{\partial \vec{J}_n}{\partial x} + (G_{net,n} - R_{net,n}) \quad (3.11)$$

$$\text{for holes, } \frac{\partial p}{\partial t} = -\frac{1}{q} \frac{\partial \vec{J}_p}{\partial x} + (G_{net,p} - R_{net,p}) \quad (3.12)$$

Where $G_{net,carrier\ type}$ is the net generation rate of the carrier, $R_{net,carrier\ type}$ is the net recombination rate of the carrier, n and p is the carrier density, and \vec{J}_n and \vec{J}_p are the total current equations for electrons and holes, respectively.

The total current equations can be given by [6],[26]

$$J_n = J_{n(drift)} + J_{n(diffusion)} = qn\mu_n\mathcal{E} + qD_n \frac{dn}{dx} \quad (3.13)$$

$$J_p = J_{p(drift)} + J_{p(diffusion)} = qn\mu_p\mathcal{E} - qD_p\frac{dn}{dx} \quad (3.14)$$

In the TCAD, these same equations are expressed by [26]

$$\vec{J}_n = \mu_n(n\nabla E_C - 1.5nkT\nabla \ln m_n) + D_n(\nabla n - n\nabla \ln \gamma_n) \quad (3.15)$$

$$\vec{J}_p = \mu_p(p\nabla E_V - 1.5pkT\nabla \ln m_p) - D_p(\nabla p - p\nabla \ln \gamma_p) \quad (3.16)$$

Where $\mu_{carrier\ type}$ is carrier mobility, $m_{carrier\ type}$ is carrier mass, $D_{carrier\ type}$ is carrier diffusion constant (same as $D = \mu kT$), $\gamma_n = \frac{n}{N_C} \exp(-\eta_n)$, $\gamma_p = \frac{p}{N_C} \exp(-\eta_p)$, $\eta_n = \frac{E_{F,n} - E_C}{kT}$, $\eta_p = \frac{E_V - E_{F,p}}{kT}$

Above equations called the Drift-Diffusion model which is normally used for the isothermal simulation devices such as MOSFET, BJT.

In this thesis, the Hydro-Dynamic model is used for the simulation. The Hydrodynamic model is basically same as the Drift model excepts it includes carrier temperature terms and lattice heat terms additionally. This model is suitable for sub-micron devices and heterointerface devices. The total current equations in the Hydrodynamic model is given by [26]

$$\vec{J}_n = \mu_n(n\nabla E_C + kT_n\nabla n - nkT_n\nabla \ln \gamma_n + \lambda_n f_n^{td} kn\nabla T_n - 1.5nkT_n\nabla \ln m_n) \quad (3.17)$$

$$\vec{J}_p = \mu_p(p\nabla E_V - kT_p\nabla p + pkT_p\nabla \ln \gamma_p - \lambda_p f_p^{td} kp\nabla T_p + 1.5pkT_p\nabla \ln m_p) \quad (3.18)$$

where T_n and T_p are the carrier temperature, a f_n^{td} and f_p^{td} are zero (default value, only in the thermo-dynamic model it can be adjusted), $\lambda_n = F_{1/2}(\eta_n)/F_{-1/2}(\eta_n)$, $\lambda_p = F_{1/2}(\eta_p)/F_{-1/2}(\eta_p)$. The performance difference between the Drift-Diffusion model and Hydro-Dynamic model is covered in chapter 4.

3.2.3.4 High-field saturation model

At high field, the carrier energy starts to scatter its energy by emission of phonon to the lattice. When vertical field, effective electric-field (\mathcal{E}_{eff}) increases, the effective mobility (μ_{eff}) drops rapidly because of surface scattering effect. This relationship can be expressed by $v_{sat} = \mathcal{E}_{eff} \times \mu_{eff}$. When electric-field (\mathcal{E}_{eff}) strength become greater than the critical electric field (\mathcal{E}_c), mobility decreases rapidly. Also, carrier velocity becomes saturated. This is drift velocity-saturation (v_{sat}). [13],[26] Thus, the current saturation of sub-micron devices starts at a much lower gate voltage, critical electric field compared that of long-channel devices.

The experimented drift-velocity model (Caughey and Thomas model) is given by [13]

$$v = \frac{\mu_{eff} \times \mathcal{E}_{eff}}{\left(1 + \left(\frac{\mathcal{E}_{eff}}{\mathcal{E}_c}\right)^n\right)^{\frac{1}{n}}} \quad (3.19)$$

Where \mathcal{E}_c is the critical field (vertical field), n is for optimizing value ($n=2$ is for electrons, $n=1$ is for holes), v is drift-velocity.

This thesis uses extended Canali model which is originated from Caughey and Thomas model for high field saturation. This equation is given by [26]

$$\mu(F) = \frac{(\alpha + 1)\mu_{low}}{\alpha + \left[1 + \left(\frac{(\alpha + 1)\mu_{low}F_{hfs}}{v_{sat}}\right)^\beta\right]^{\frac{1}{\beta}}} \quad (3.20)$$

Where $\mu(F)$ is mobility at high electric-field, μ_{low} is a low electric field, F_{hfs} is driving force, v_{sat} is drift saturation velocity, α and β are smoothing values. Among several kinds of driving force model, Hydro-dynamic driving force is used which is given by [26]

$$F_{hfs,n} = \sqrt{\frac{\max(w_n - w_0, 0)}{\tau_{e,n} q \mu_n}} \quad (3.21)$$

Where $w_n = 3kT_n/2$ is the average electron energy, $w_0 = 3kT/2$ is the equilibrium thermal energy, and $\tau_{e,n}$ is the energy relaxation time.

The above equation includes electron energy terms because of the consideration of the velocity overshoot. The velocity overshoot happens at the submicron devices. Under high-field some carriers, hot carriers, get higher energy than that of nearby lattices. Hot carriers exceed its carrier saturation velocity (v_{sat}) and no longer keep thermal equilibrium. This velocity overshoot behavior is not described properly in drift-diffusion model. Thus, this thesis uses the high-field saturation model using hydrodynamic driving force model. [13],[26] For using the Hydrodynamic model, the codes for the high-field saturation with sub-model, CarrierTempDrive and eTemperature in the Solve section must be activated. Appendix B includes these codes.

3.2.4 Recombination model

Radiative, Auger and Shockley-Read Hall(SRH) models are used for recombination process. During recombination of electron and hole, its energy is released or transferred to the lattice for making energy equilibrium states. The radiative model describes the emission of phonon to release its energy. Auger process is transferred carrier energy to the third particle. Shockley–Read–Hall (SRH) process is conducted at impurities or trap. [26]

Chapter 4

THE MODEL DESCRIPTION AND RESULTS

4.1 The Simulation Platform

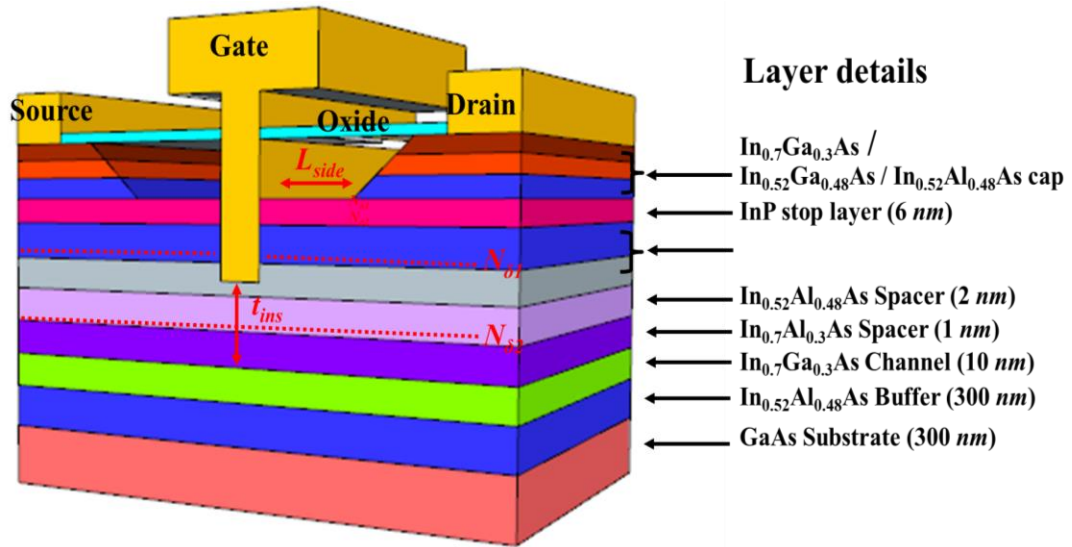


Figure 4.1: The Schematic of the InGaAs channel HEMT.

The structure of the transistor under this study is shown in Figure 4.1. It consists of a 20 nm of $\text{In}_{0.7}\text{Ga}_{0.3}\text{As} / \text{In}_{0.52}\text{Ga}_{0.48}\text{As} / \text{In}_{0.52}\text{Al}_{0.49}\text{As}$ multi-cap layers, 6 nm of the InP etching stop layer, 8 nm of the $\text{In}_{0.52}\text{Al}_{0.48}\text{As}$ barrier layer, 3 nm of the $\text{In}_{0.52}\text{Al}_{0.48}\text{As} / \text{In}_{0.7}\text{Al}_{0.3}\text{As}$ spacer layers, and 10 nm of the $\text{In}_{0.7}\text{Ga}_{0.3}\text{As}$ channel, 300 nm of the $\text{In}_{0.52}\text{Al}_{0.48}\text{As}$ buffer and 300 nm of the GaAs substrate (from top to bottom).

Figure 4.2 is the schematic of the simulation structure. The DC curves of this simulation match the experimental data previously conducted by D.H. Kim, *et al.* [21]

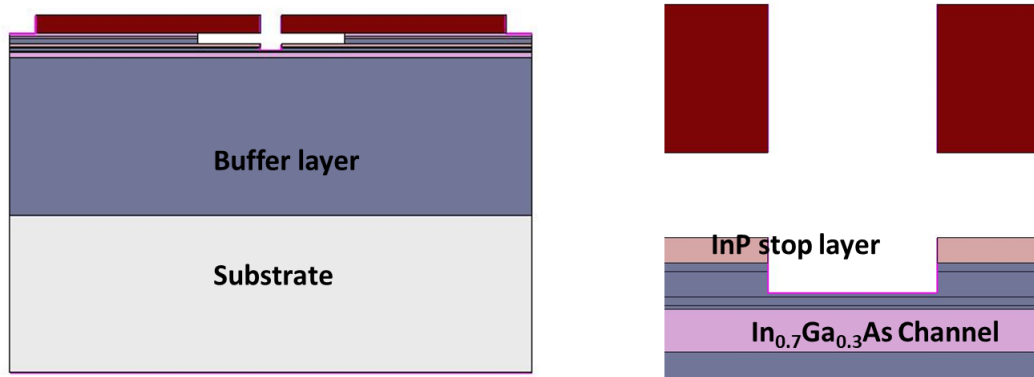


Figure 4.2: The schematic of the simulation structure.

To develop a reliable simulation model, it was compared to the current published experimental data. In the published data the distance between the source and drain is $2 \mu m$. In this simulation, the distance between source and drain is reduced to the $1 \mu m$ for reducing the calculation time. The simulation results depending on the distance between source and drain is negligible.

Figure 4.3(a), (b), and (c) show the mesh size, I_D vs V_{DS} , and I_D vs V_{GS} graph depending on mesh size respectively.

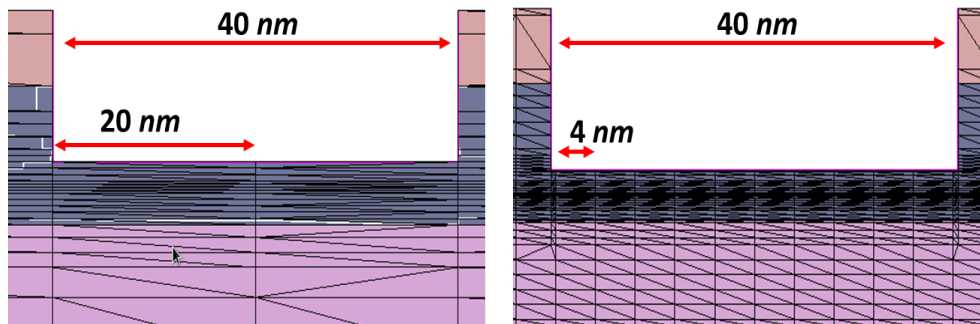


Figure 4.3(a): The mesh size below the gate region.

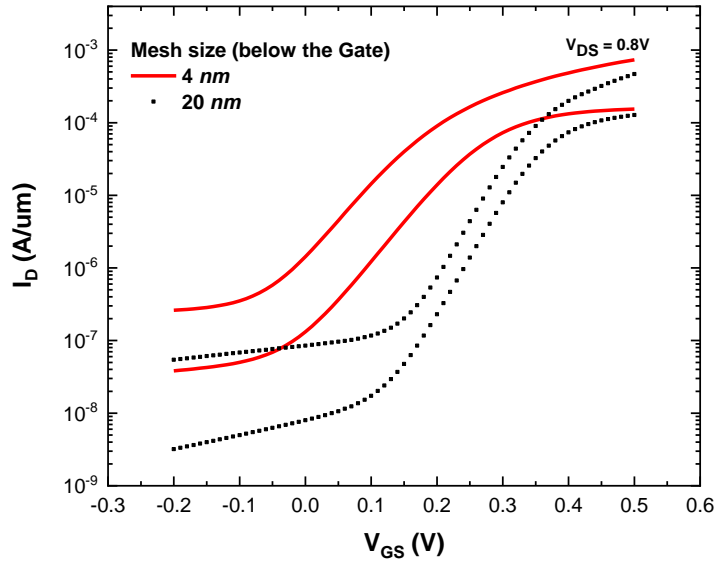


Figure 4.3(b): The I_D vs V_{GS} curve depending on mesh size.

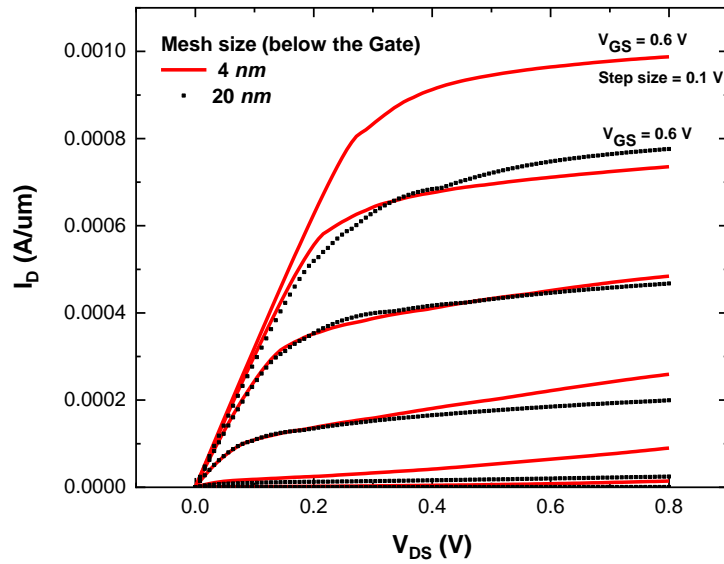


Figure 4.3(c): The I_D vs V_{DS} curve depending on mesh size.

As mentioned Chapter 3, the dense mesh setting precisely describes the device characteristics. The mesh size below the gate region is an active region, the barrier, spacer, and the channel layers. Thus, setting the smaller size of the mesh is important. Figure 4.3(b) shows the dramatic change of subthreshold depending on the mesh size. Figure 4.3(c) presents the problem of the larger mesh size. In the larger mesh size graph, the short-channel effect is not described even though gate length is 40 nm.

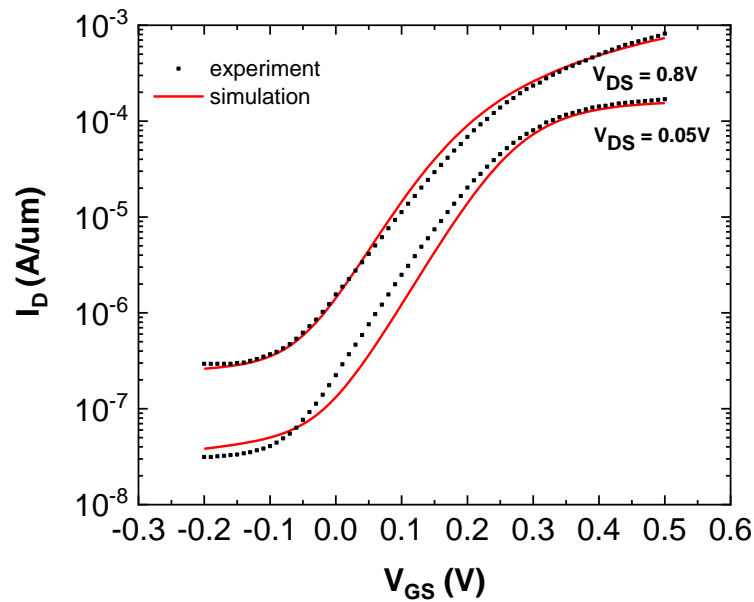


Figure 4.4(a): The comparison of I_D vs V_{GS} with simulation results and experimental data.

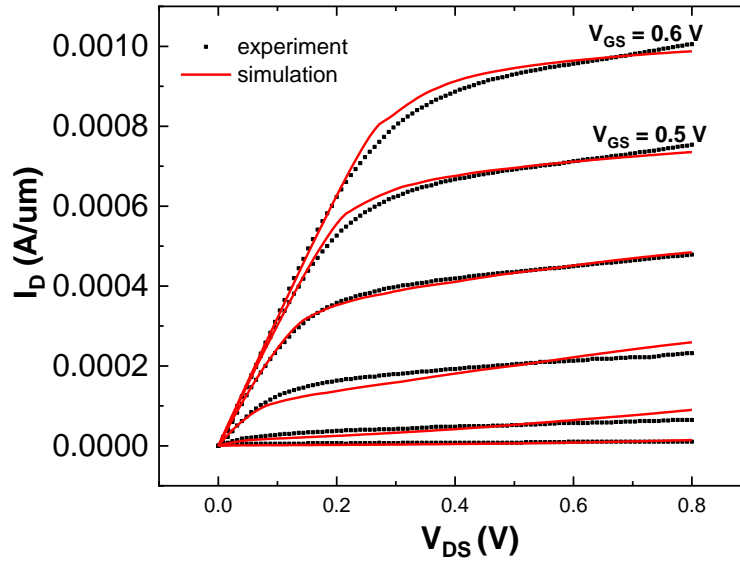


Figure 4.4(b): The comparison of I_D vs V_{DS} with simulation results and experimental data .

Figure 4.4(a),(b) presents the comparison of I_D vs V_{GS} , and I_D vs V_{DS} with simulation results and experimented data respectively. The two delta-doping layers with sheet densities of $N_{\delta 1}$ and $N_{\delta 2}$ are assigned to the barrier layer as shown in Figure 1. Afterward, the material parameters in the sentaurus simulation are adjusted accordingly. The electron mobility for various doping concentrations and high-field saturation model are modified according to the On-current. The agreement of subthreshold slope (SS) is observed. A band to band recombination model is added to fit the experimental Off-current. The Schottky barrier height is set to $0.83 eV$ to fit the threshold voltage. The agreement indicates the perfect accuracy of our TCAD simulation in all operating regions.

4.2 Model Descriptions and Results

One of the main benefits of the HEMT simulation is how to improve performance by optimizing its structure. Based on the developed TCAD simulation platform, various structural parameters are discussed in this section.

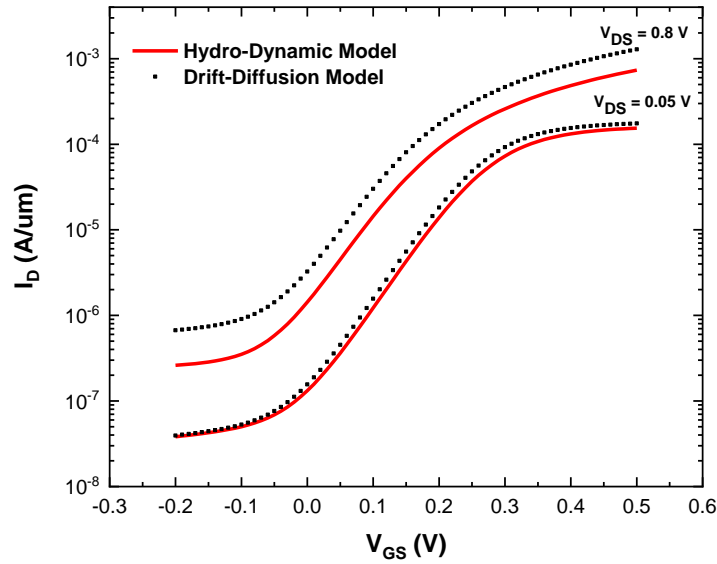


Figure 4.5(a): The comparison of I_D vs V_{GS} depending on carrier transport model.

Figure 4.5(a), (b) shows the comparison of I_D vs V_{GS} , and I_D vs V_{DS} depending on carrier transport models. In the Drift-Diffusion model, the short channel effect is overestimated. Figure 4.5(a) presents the increased DIBL in the Drift-Diffusion model. Figure 4.5(b) indicates the overestimated velocity overshoot effect. The I_D vs V_{DS} curve is not saturated compared to experimented data.

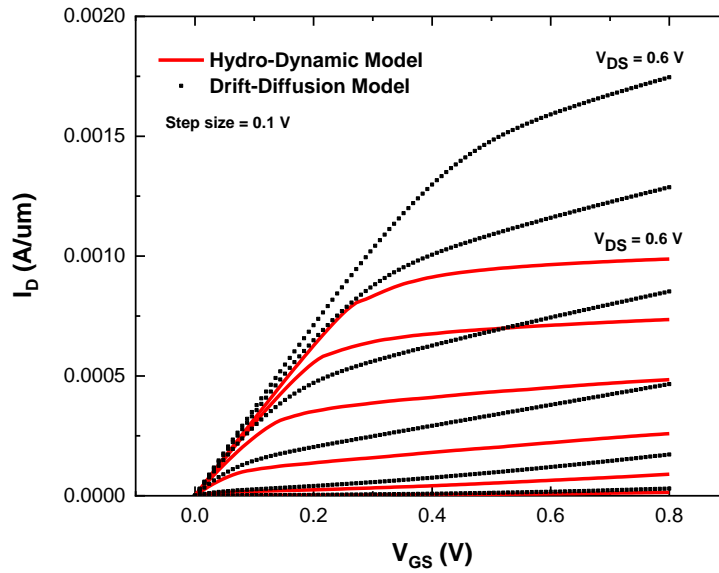


Figure 4.5(b): The comparison of I_D vs V_{DS} depending on carrier transport model.

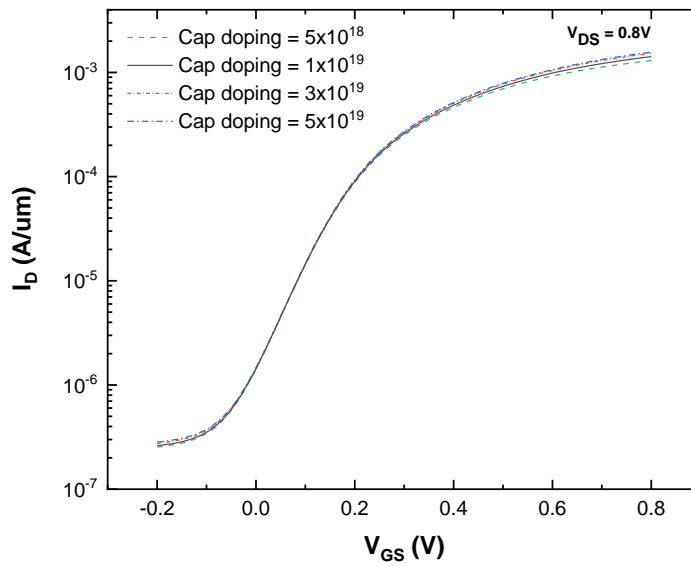


Figure 4.6: The comparison of I_D vs V_{GS} depending on the cap doping concentration.

Figure 4.6 presents the comparison of I_D vs V_{GS} at $V_{DS} = 0.8$ V depending on the cap doping concentrations. This simulation uses the doping concentration, $1 \times 10^{19} \text{ cm}^{-3}$. This value is a reasonable doping concentration for real fabrication. Besides, with heavy dope concentration, the contact interface of metal and semiconductor becomes an ohmic contact. Thus, proportionally increased current well describes the low resistive condition.

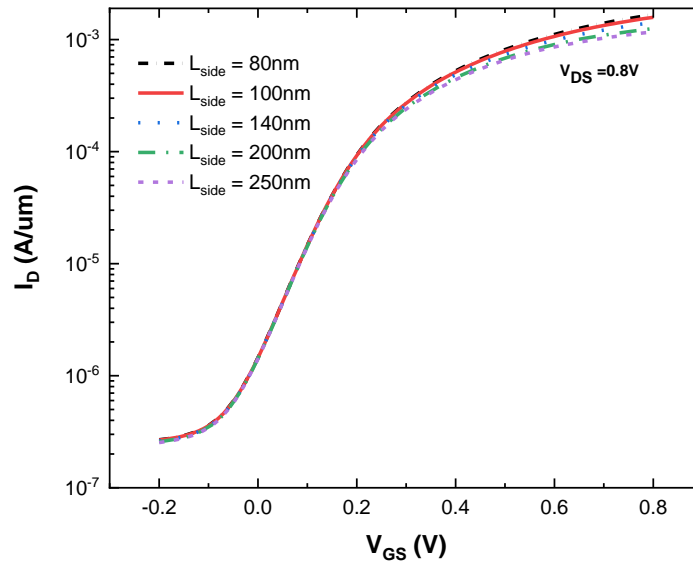


Figure 4.7: The I_D vs V_{GS} curves for various length of L_{side} .

In Figure 4.7, the I_D vs V_{GS} curves are compared depending on a transistor with different gate-to-drain recessing etching distances (L_{side}). It shows that the On-current will increase with a shorter L_{side} , while the Off-current stays the same, suggesting a parasitic resistance behavior. [29],[30]

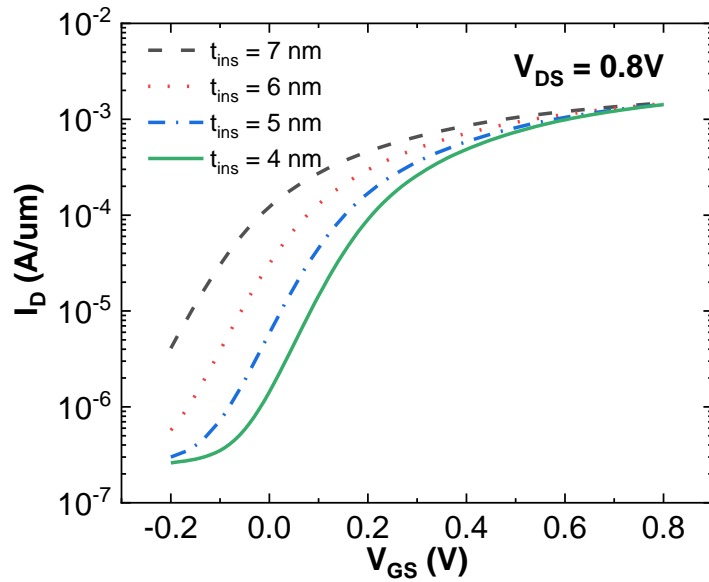


Figure 4.8: The I_D vs V_{GS} for various values of t_{ins} .

Figure 4.8 indicates that reducing the distance of the gate-to-channel (t_{ins}) will result in a lower SS, in agreement with the experimental data, suggesting a better gate control. Thus, by reducing the barrier thickness, the ratio of I_{on}/I_{off} is increased but the overall current is dropped. [31]

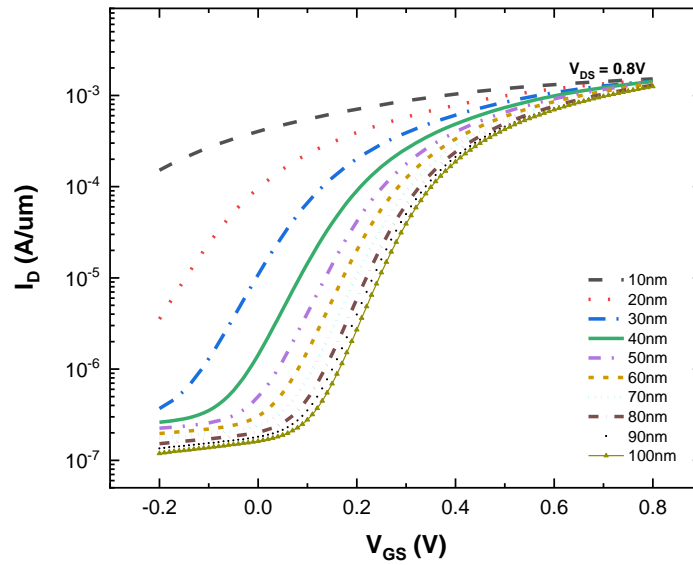


Figure 4.9: I_D vs V_{GS} curves for various length of L_{gate} .

Figure 4.9 shows the I_D vs V_{GS} curves for various length of L_{gate} . The lower SS is 79 mV/dec at $L_{gate} = 100 \text{ nm}$. The amount of charge, which the gate can control decreases as channel length decreases due to source and drain bias.

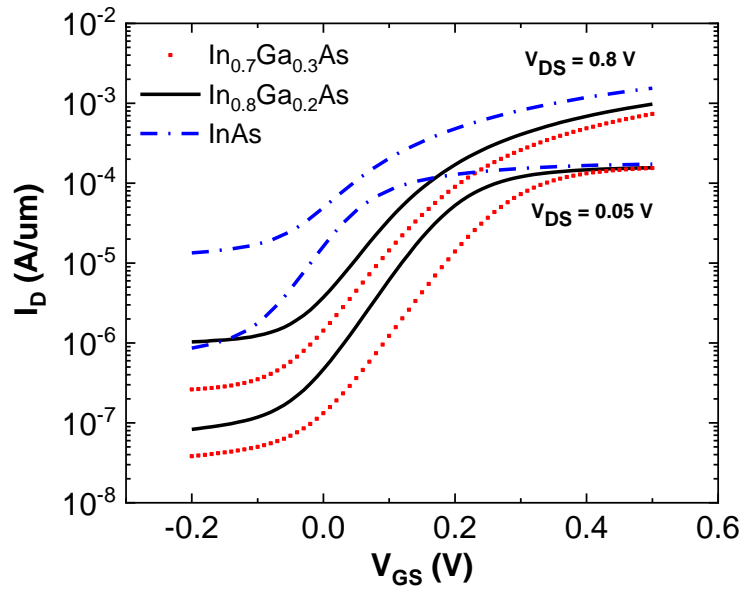


Figure 4.10(a): I_D vs V_{GS} curves for HEMT with different Indium mole fraction.

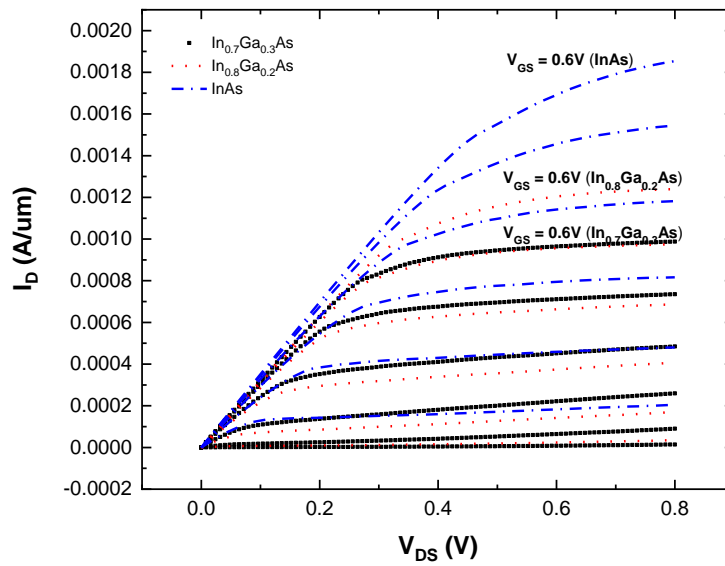


Figure 4.10(b): I_D vs V_{DS} curves for HEMT with different Indium mole fraction.

Figure 4.10(a),(b) show the I_D vs V_{GS} and I_D vs V_{DS} curves of the transistor with different Indium mole fractions respectively. Considering the lattice mismatch, the channel thickness is reduced depending on the mole fraction. The thickness of channels is 7 nm for $\text{In}_{0.8}\text{Ga}_{0.2}\text{As}$, 4 nm for InAs respectively while the original $\text{In}_{0.7}\text{Ga}_{0.3}\text{As}$ channel thickness is 10 nm.

The higher On-current is achieved by increasing the channel's Indium mole fraction because of the increased mobility indicated in Figure 4.10(a) and 4.10(b). However, the Off-current increases because of the simultaneously decreased tunneling mass in Figure 4.10(a). Thus, there is a tradeoff between higher I_{on} and I_{on}/I_{off} .

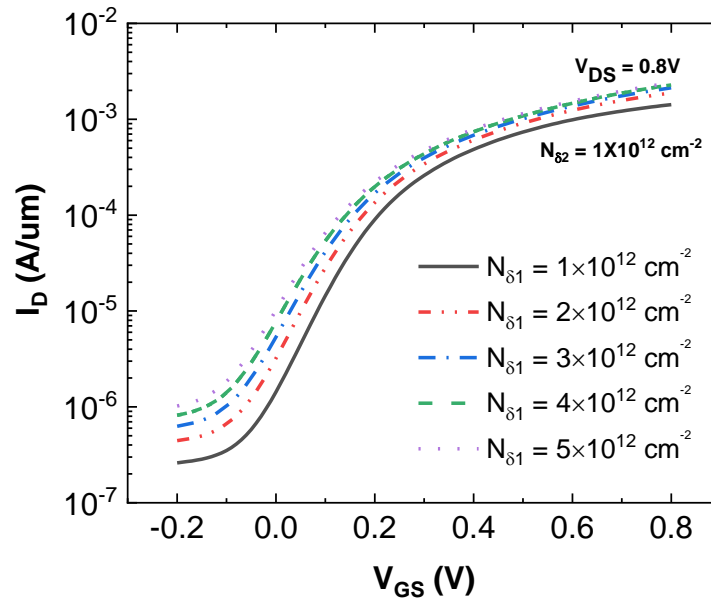


Figure 4.11(a): The I_D vs V_{GS} curves for various values of $N_{\delta 1}$.

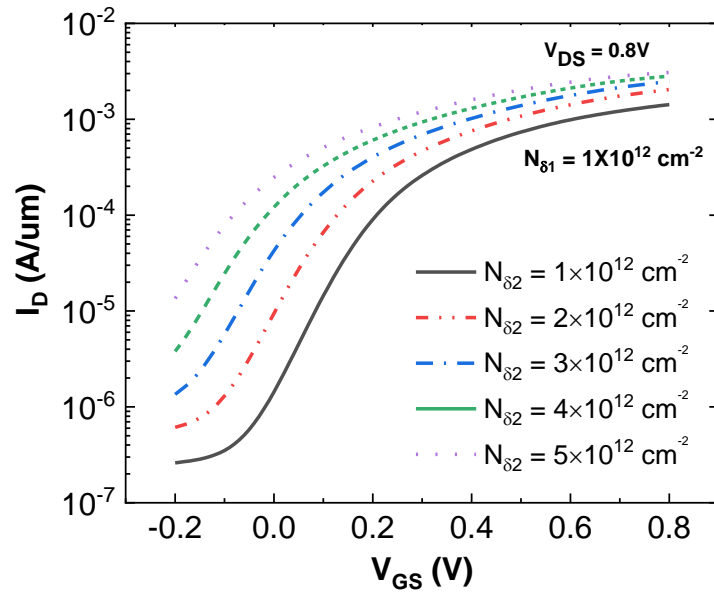


Figure 4.11(b): The I_D vs V_{GS} curves for various values of $N_{\delta 2}$.

Figure 4.11(a),(b) show the impact of $N_{\delta 1}$ and $N_{\delta 2}$ on the I_D vs V_{GS} curves. It should be noted that the I_D vs V_{GS} curves are more sensitive to the $N_{\delta 2}$ because the bottom delta doping is closer to the channel region.

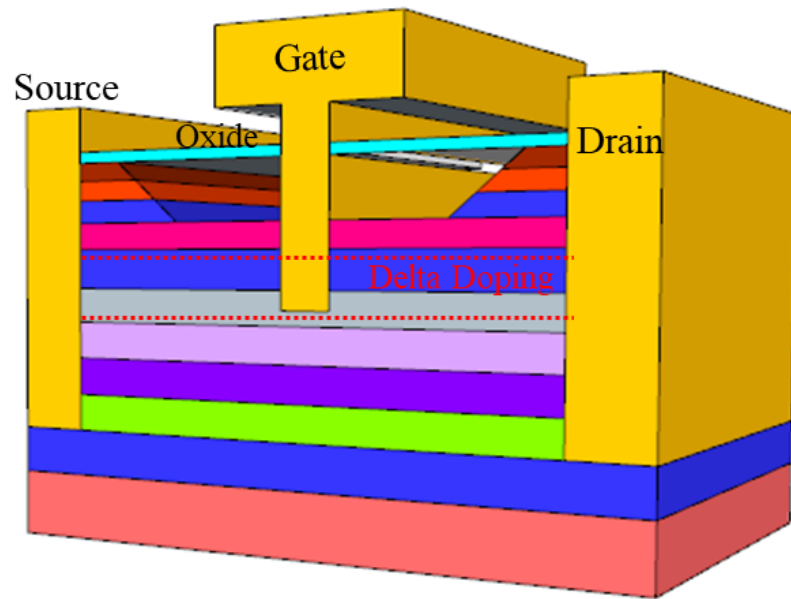


Figure 4.12: The Schematic for buried S/D for HEMT.

Finally, the schematic for buried S/D contact in the HEMT simulation for the improved Off-current is shown in Figure 4.12. The S/D contacts are placed directly on the InAlAs buffer layer. The delta-doping concentration is modified. To maintain the off-current $N_{\delta 1}$ value is decreased, and to increase the current $N_{\delta 2}$ value is increased compared to the original simulation model.

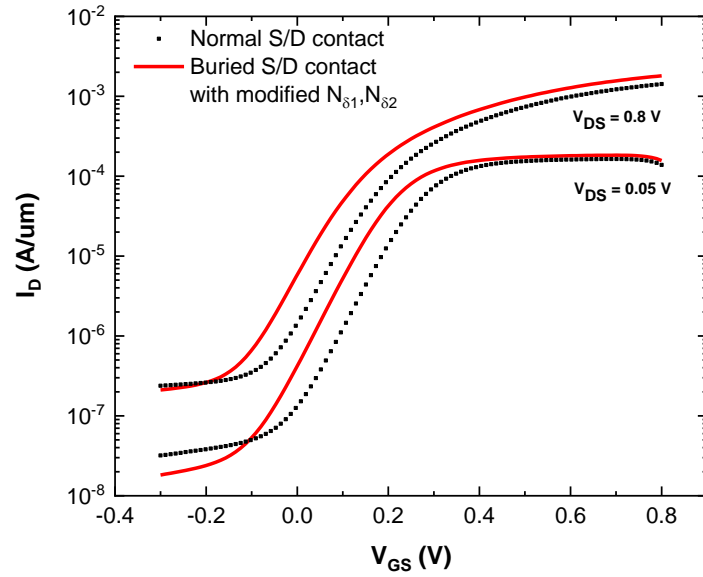


Figure 4.13(a): Comparison of simulation performance with normal S/D and buried S/D.

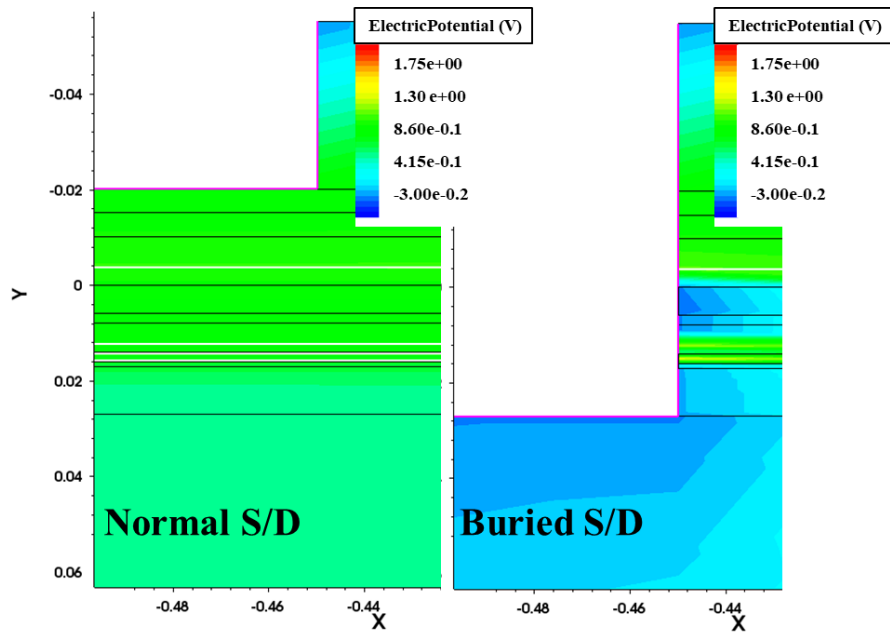


Figure 4.13(b): Comparison of simulation performance with normal S/D and buried S/D.

As indicated in Figure 4.13(a), the benefit of this structure is a lower Off-current while the On-current maintains the same level. This phenomenon results from a lower electric potential of the substrate as observed in Figure 4.13(b), which leads to the reduced electron density in the subthreshold region. The buried source/drain structure with modified $N_{\delta 1}$ and $N_{\delta 2}$ shows the lower Off-current and improved SS from 97 mV/dec to 90 mV/dec at $V_{DS} = 0.8 \text{ V}$ in Figure 4.13(a).

Chapter 5

CONCLUSION

With the development of millimeter wave technology, optical communication, satellites and radars, the needs of high-speed and -frequency devices have emerged. InGaAs-channel based High Electron Mobility Transistor (HEMT) is widely viewed as the best candidate for future low-noise GHz applications. HEMT using the heterojunction bandgap enhances the device speed due to its higher mobility and increased transconductance. HEMT's enhanced performance results from 2DEG region. Therefore, it can confine electrons and has higher conductivity.

The Molecular Beam Epitaxy (MBE) process is required to make abrupt heterojunction and delta-doped layers for the HEMTs. The MBE process enables fabricating the high-speed device using ultra-high-vacuum and fine control of dopant for III-V compounds materials. However, this process takes labor to control the substrate and requires extensive experimenting to make flawless junctions and compositions.

This thesis develops a simulation model to predict the device performance and optimization of design in addition to saving time and cost. In this thesis, optimizations using double-delta doping above the channel with simulation set-up is reported. The simulation results show higher On-current and Off-current with increased Indium mole fraction in the channel. It shows that the Off-current is reduced by 10% and On-current is increased by 26% at a high drain voltage bias, Off-current is half of the normal structure and On-current is increased by 11% at a low voltage bias after utilization of these methods. The SS is reduced to 90 mV/dec with optimized delta-doping.

REFERENCES

1. D.-H. Kim and J. A. del Alamo, "30-nm InAs pseudomorphic HEMTs on an InP substrate with a current-gain cutoff frequency of 628 GHz," *IEEE Electron Device Lett.*, vol. 29, no. 8, pp. 830–833, Aug. 2008.
2. T. Takahashi, Y. Kawano, K. Makiyama, S. Shiba, M. Sato, Y. Nakasha, and N. Hara, "Enhancement of f_{max} to 910 GHz by Adopting Asymmetric Gate Recess and Double-Side-Doped Structure in 75-nm Gate InAlAs/InGaAs HEMTs," *IEEE Transactions on Electron Devices*, Vol. 64, No. 1, pp. 89–94, 2017.
3. K. Shinohara, Y. Yamashita, A. Endoh, I. Watanabe, K. Hikosaka, T. Matsui, T. Mimura, and S. Hiyamizu, "547 GHz $\text{In}_{0.7}\text{Ga}_{0.3}\text{As}/\text{In}_{0.52}\text{Al}_{0.48}\text{As}$ HEMTs with reduced source and drain resistance," *IEEE Electron Device Lett.*, vol. 25, no. 5, pp. 241–243, May 2004.
4. S.M.SZE, *High-Speed Semiconductor Devices*. New York: Wiley, 1990.
5. S. Adachi, *Properties of group-IV, III-V and II-VI semiconductors*. Chichester: John Wiley & Sons, 2005.
6. D. A. Neamen, *Semiconductor physics and devices: basic principles*, 4th ed. New York, NY: McGraw-Hill, 2012.
7. M. Kawano, T. Kuzuhara, H. Kawasaki, F. Sasaki, and H. Tokuda, "InAlAs/InGaAs metamorphic low noise HEMT," *IEEE Microwave Guided Wave Lett.*, vol. 7, pp. 6–8, 1997.
8. K. Inoue, J. C. Hannand, and T. Matsuno, "High-quality $\text{In}_x\text{Ga}_{1-x}\text{As}/\text{InAlAs}$ modulation-doped heterostructures grown lattice-mismatched on GaAs substrates," *J. Crystal Growth*, vol. 111, pp. 313–317, 1991.
9. P. Roblin and H. Rohdin, *High-speed heterostructure: from device concepts to circuit modeling*. Cambridge: Cambridge University Press, 2001.
10. L. L. Chang and K. Ploog, *Molecular beam epitaxy and heterostructures*. Dordrecht: M. Nijhoff, 1985.
11. A. Brown, *VLSI Circuits and Systems in Silicon*. London: McGraw-Hill Book Company, 1991.

12. C. Mead and L. Conway, *Introduction to VLSI Systems*. Addison-Wesley, 1980.
13. Y. Taur and T. H. Ning, *Fundamentals of modern VLSI devices*. Cambridge: Cambridge Univ. Press, 1998.
14. B. L. Anderson and R. L. Anderson, *Fundamentals of semiconductor devices*, 2nd ed. 2018.
15. C. T. Wang, *Introduction to semiconductor technology: GaAs and related compounds*. New York: Wiley, 1990.
16. R. Goyal, *High-frequency analog integrated circuit design*. New York: John Wiley & Sons, 1995.
17. M. S. Shur, *GaAs devices and circuits*. New York : Plenum Press, 1987.
18. E. F. Schubert, *Delta-doping of semiconductors*. Cambridge: Cambridge Univ. Press, 1996.
19. J. Mun, *GaAs integrated circuits*: Oxford: BSP Professional Books, 1988.
20. E.-Y. Chang *et al.*, “InAs thin-channel high-electron-mobility transistors with very high current-gain cutoff frequency for emerging submillimeter-wave applications,” *Appl. Phys. Exp.*, vol. 6, no. 3, p. 034001, 2013.
21. D.-H. Kim, B. Brar, and J. del Alamo, “ $f_T = 688$ GHz and $f_{MAX} = 800$ GHz in $L_g = 40$ nm $In_{0.7}Ga_{0.3}As$ MHEMTs with $g_{m,max} > 2.7$ mS/ μm ,” in *IEDM Tech. Dig.*, 2011, pp. 13.6.1–13.6.4.
22. D. A. J. Moran, K. Kalna, E. Boyd, F. McEwan, H. McLelland, L. L. Zhuang, C. R. Stanley, A. Asenov, and I. Thayne, “Self-aligned $0.12 \mu m$ T-gate $In_{0.53}Ga_{0.47}As/In_{0.52}Al_{0.48}As$ HEMT technology utilising a non-annealed ohmic contact strategy,” in *Proc. 35th ESSDERC*, J. Franca and P. Freitas, Eds., Estoril, Portugal, 2003 pp. 315–318.
23. A. Endoh, Y. Yamashita, K. Shinohara, K. Hikosaka, T. Matsui, S. Hiyamizu, and T. Mimura, “InP-based high electron mobility transistors with a very short gate-channel distance,” *Jpn. J. Appl. Phys.*, vol. 42, no. 4B, pp. 2214–2218, Apr. 2003.

24. Y. Yamashita, A. Endoh, M. Higashiwaki, K. Hikosaka, T. Mimura, S. Hiyamizu, and T. Matsui, "High f_T 50-nm-gate InAlAs/InGaAs high electron mobility transistors lattice-matched to InP substrates," *Jpn. J. Appl. Phys.*, vol. 39, pp. L838–L840, 2000.
25. P. Smith, S.-M. Liu, M.-Y. Kao, P. Ho, S. Wang, K. Duh, S. Fu, and P. Chao, "W-Band high efficiency InP-based power HEMT with 600 GHz f_{max} ," *IEEE Microwave Guided Wave Lett.*, vol. 5, pp. 230–232, 1995.
26. Synopsys. TCAD Sentaurus User Guide, Version N-2017.09, September 2017.
27. Y. Fu, Z. Li, W. T. Ng, and J. K. O. Sin, *Integrated Power Devices and Tcad Simulation*. Boca Raton : CRC Press, 2014.
28. J. C. Harmand, T. Matsuno, and K. Inoue, "Lattice-mismatched growth and transport properties of InAlAs/InGaAs heterostructures on GaAs substrates," *Jpn. J. Appl. Phys.*, vol. 28, no. Part 2, no. 7, pp. L1101–L1103, Jul. 1989.
29. K. J. Chen, T. Enoki, K. Maewawa, K. Arai, and M. Yamamoto, "High performance InP-based enhancement-mode HEMTs using non-alloyed ohmic contact and Pt-based buried-gate technologies," *IEEE Trans. Electron Devices*, vol. 43, no. 2, pp. 252–257, Feb. 1996.
30. D.-H. Kim, J. A. del Alamo, J.-H. Lee, and K.-S. Seo, "The impact of side-recess spacing on the logic performance of 50 nm In_{0.7}Ga_{0.3}As HEMTs," in *Proc. 18th IEEE IPRM Conf.*, May 2006, pp. 177–180.
31. D.-H. Kim and J. A. del Alamo, "Lateral and vertical scaling of In_{0.7}Ga_{0.3}As HEMTs for post-Si-CMOS logic applications," *IEEE Trans. Electron Devices*, vol. 55, no. 10, pp. 2546–2553, Oct. 2008.

Appendix A

THE STRUCTURE CODES

Appendix A shows the simulated HEMT structure. These codes include device structure, doping profile, and mesh strategy.

```
(sdegeo:set-default-boolean "ABA")
```

;etch stopper layer

```
(sdegeo:create-rectangle (position 0.0 0.0 0.0) (position @Ltot@ @Hstop@ 0.0) "InP" "stop")
```

;barrier1 layer

```
(sdegeo:create-rectangle (position 0.0 @Hstop@ 0.0) (position @Ltot@ (+ @Hstop@ @Hba1@) 0.0) "InAlAs" "barrier1")
```

;barrier2 layer

```
(sdegeo:create-rectangle (position 0.0 (+ @Hstop@ @Hba1@) 0.0) (position @Ltot@ (+ @Hstop@ @Hba1@ @Hba2@) 0.0) "InAlAs" "barrier2")
```

;spacer1 layer

```
(sdegeo:create-rectangle (position 0.0 (+ @Hstop@ @Hba1@ @Hba2@) 0.0) (position @Ltot@ (+ @Hstop@ @Hba1@ @Hba2@ @Hspacer1@) 0.0) "InAlAs" "spacer1")
```

;spacer2 layer

```
(sdegeo:create-rectangle (position 0.0 (+ @Hstop@ @Hba1@ @Hba2@ @Hspacer1@) 0.0) (position @Ltot@ (+ @Hstop@ @Hba1@ @Hba2@ @Hspacer1@ @Hspacer2@) 0.0) "InAlAs" "spacer2")
```

;channel layer

(sdegeo:create-rectangle (position 0.0 (+ @Hstop@ @Hba1@ @Hba2@ @Hspacer1@ @Hspacer2@) 0.0) (position @Ltot@ (+ @Hstop@ @Hba1@ @Hba2@ @Hspacer1@ @Hspacer2@ @Hch@) 0.0) "InGaAs" "channel")

;buffer layer

(sdegeo:create-rectangle (position 0.0 (+ @Hstop@ @Hba1@ @Hba2@ @Hspacer1@ @Hspacer2@ @Hch@) 0.0) (position @Ltot@ (+ @Hstop@ @Hba1@ @Hba2@ @Hspacer1@ @Hspacer2@ @Hch@ @Hbu@) 0.0) "InAlAs" "buffer")

;substrate layer

(sdegeo:create-rectangle (position 0.0 (+ @Hstop@ @Hba1@ @Hba2@ @Hspacer1@ @Hspacer2@ @Hch@ @Hbu@) 0.0) (position @Ltot@ (+ @Hstop@ @Hba1@ @Hba2@ @Hspacer1@ @Hspacer2@ @Hch@ @Hbu@ @Hsub@) 0.0) "GaAs" "substrate")

;cap layer1

(sdegeo:create-rectangle (position @Lside@ 0.0 0.0) (position @Ltot@ (- 0 @Hcap1@) 0.0) "InAlAs" "cap1")

;cap layer2

(sdegeo:create-rectangle (position @Lside@ (- 0 (+ @Hcap1@)) 0.0) (position @Ltot@ (- 0 (+ @Hcap1@ @Hcap2@)) 0.0) "InGaAs" "cap2")

;cap layer3

(sdegeo:create-rectangle (position @Lside@ (- 0 (+ @Hcap1@ @Hcap2@)) 0.0) (position @Ltot@ (- 0 (+ @Hcap1@ @Hcap2@ @Hcap3@)) 0.0) "InGaAs" "cap3")

;oxide

(sdegeo:create-rectangle (position 0.0 (- 0 (+ @Hcap1@ @Hcap2@ @Hcap3@)) 0.0)

```

(position @Ltot@ (- 0 (+ @Hcap1@ @Hcap2@ @Hcap3@ @Hox@)) 0.0) "SiO2"
"oxide")

;gate

(sdegeo:create-rectangle (position 0.0 -0.3 0.0) (position (/ @Lgate@ 2) (+ @Hstop@
@tins@) 0.0) "Metal" "gate")

;drain

(sdegeo:create-rectangle (position @Ld@ (- 0 (+ @Hcap1@ @Hcap2@ @Hcap3@))
0.0) (position @Ltot@ (- 0 (+ @Hcap1@ @Hcap2@ @Hcap3@ 0.05)) 0.0) "Metal"
"drain")

(define tr1 (transform:reflection (position 0 0 0) (gvector 0 -1 0)))
(set! tr1 (transform:reflection (position 0 0 0) (gvector 1 0 0)))
(sdegeo:mirror-selected (get-body-list) tr1 #t)

;(define gate1 (sdegeo:create-rectangle (position (- 0 (/ @Lgate@ 2)) -0.3 0.0)
(position (/ @Lgate@ 2) (+ @Hstop@ @tins@) 0.0) "Metal" "gate1"))

(define drain1 (sdegeo:create-rectangle
  (position @Ld@ (- 0 (+ @Hcap1@ @Hcap2@ @Hcap3@)) 0.0)
  (position @Ltot@ (- 0 (+ @Hcap1@ @Hcap2@ @Hcap3@ 0.05)) 0.0) "Metal"
  "drain1"))

(sdegeo:define-contact-set "g" 4 (color:rgb 1 0 0) "##" )
(sdegeo:define-contact-set "d" 4 (color:rgb 0 1 0) "##" )
(sdegeo:define-contact-set "s" 4 (color:rgb 0 0 1) "##" )
(sdegeo:define-contact-set "b" 4 (color:rgb 1 1 0) "##")
(sdegeo:set-current-contact-set "g")
(sdegeo:set-contact-boundary-edges gate1)

```

```

(sdegeo:delete-region gate1)
(sdegeo:set-current-contact-set "d")
(sdegeo:set-contact-boundary-edges drain1)
(sdegeo:delete-region drain1)
(define source1 (sdegeo:create-rectangle
  (position (- 0 @Ld@) (- 0 (+ @Hcap1@ @Hcap2@ @Hcap3@)) 0.0)
  (position (- 0 @Ltot@) (- 0 (+ @Hcap1@ @Hcap2@ @Hcap3@ 0.05)) 0.0)
  "Metal" "source1"))
(sdegeo:set-current-contact-set "s")
(sdegeo:set-contact-boundary-edges source1)
(sdegeo:delete-region source1)
(sdegeo:set-current-contact-set "b")
(sdegeo:define-2d-contact ( list( car( find-edge-id( position 0.0 (+ @Hstop@ @Hba1@
  @Hba2@ @Hspacer1@ @Hspacer2@ @Hch@ @Hbu@ @Hsub@) 0.0)))) "b")
;profile
(define YDelta 0.012)
(display "Location of Delta-Doping layer: ") (display YDelta) (display "um")
(define DeltaThick 0.0008)
(display "Thickness of Delta-Doping layer: ") (display DeltaThick) (display "um")
(define SheetCharge 1e12)
(display "SheetCharge: ") (display SheetCharge) (display "cm-2")
(define SheetCharge1 1e12)
(display "SheetCharge1: ") (display SheetCharge1) (display "cm-2")
(sdedr:define-refinement-window "BaseLine.Delta" "Line"

```

```

(position (* @Ltot@ -1.0) YDelta 0.0)
(position (* @Ltot@ 2.0) YDelta 0.0)
(sdedr:define-gaussian-profile "Prof.Delta"
"ArsenicActiveConcentration"
"PeakPos" 0 "PeakVal" (* (/ SheetCharge DeltaThick) 3e4)
"Length" (* 0.5 DeltaThick)
"Gauss" "Factor" 0.0)
(sdedr:define-analytical-profile-placement "Place.Delta"
"Prof.Delta" "BaseLine.Delta" "Both" "NoReplace" "Eval")
(define YDelta1 0.015)
(display "Location of Delta-Doping layer: ") (display YDelta1) (display "um")
(sdedr:define-refinement-window "BaseLine.Delta1" "Line"
(position (* @Ltot@ -1.0) YDelta1 0.0)
(position (* @Ltot@ 2.0) YDelta1 0.0) )
(sdedr:define-gaussian-profile "Prof.Delta1"
"ArsenicActiveConcentration"
"PeakPos" 0 "PeakVal" (* (/ SheetCharge1 DeltaThick) 2e4)
"Length" (* 0.5 DeltaThick)
"Gauss" "Factor" 0.0)
(sdedr:define-analytical-profile-placement "Place.Delta1"
"Prof.Delta1" "BaseLine.Delta1" "Both" "NoReplace" "Eval")
(sdeaxisaligned:set-parameters "yCuts"
(list (+ YDelta1 (* 2.00 DeltaThick)) (+ YDelta1 (* 1.50 DeltaThick))
(+ YDelta1 (* 1.25 DeltaThick))

```

```

(+ YDelta1 (* 1.00 DeltaThick))
(+ YDelta1 (* 0.75 DeltaThick))
(+ YDelta1 (* 0.50 DeltaThick))
(+ YDelta1 (* 0.25 DeltaThick))
(+ YDelta1 (* 0.125 DeltaThick))
YDelta1
(- YDelta1 (* 0.125 DeltaThick))
(- YDelta1 (* 0.25 DeltaThick))
(- YDelta1 (* 0.50 DeltaThick))
(- YDelta1 (* 0.75 DeltaThick))
(- YDelta1 (* 1.00 DeltaThick))
(- YDelta1 (* 1.25 DeltaThick))
(- YDelta1 (* 1.50 DeltaThick))
(- YDelta1 (* 2.00 DeltaThick))))
(sdedr:define-constant-profile                                "ConstantProfileDefinition_1"
"ArsenicActiveConcentration" 1e+19)
(sdedr:define-constant-profile-region                        "ConstantProfilePlacement_1"
"ConstantProfileDefinition_1" "cap1")
(sdedr:define-constant-profile                                "ConstantProfileDefinition_2"
"ArsenicActiveConcentration" 1e+19)
(sdedr:define-constant-profile-region                        "ConstantProfilePlacement_2"
"ConstantProfileDefinition_2" "cap1_t18")
(sdedr:define-constant-profile                                "ConstantProfileDefinition_3"
"ArsenicActiveConcentration" 1e+19)

```

```

(sdedr:define-constant-profile-region                                "ConstantProfilePlacement_3"
"ConstantProfileDefinition_3" "cap2")

(sdedr:define-constant-profile                                    "ConstantProfileDefinition_4"
"ArsenicActiveConcentration" 1e+19)

(sdedr:define-constant-profile-region                                "ConstantProfilePlacement_4"
"ConstantProfileDefinition_4" "cap2_t20")

(sdedr:define-constant-profile                                    "ConstantProfileDefinition_5"
"ArsenicActiveConcentration" 1e+19)

(sdedr:define-constant-profile-region                                "ConstantProfilePlacement_5"
"ConstantProfileDefinition_5" "cap3")

(sdedr:define-constant-profile                                    "ConstantProfileDefinition_6"
"ArsenicActiveConcentration" 1e+19)

(sdedr:define-constant-profile-region                                "ConstantProfilePlacement_6"
"ConstantProfileDefinition_6" "cap3_t22")

```

;- Meshing

```

;-----#
(sdedr:define-refinement-window "RWin.Cap" "Rectangle"
    (position @Lside@ 0.0 0.0)
    (position 0.175 (- 0 (+ @Hcap1@ @Hcap2@ @Hcap3@)) 0.0) )
(sdedr:define-refinement-size "Ref.Cap"
    (/ @Ltot@ 2.0) (/ (+ @Hcap1@ @Hcap2@ @Hcap3@) 1.0)
    (/ @Ltot@ 4.0) (/ (+ @Hcap1@ @Hcap2@ @Hcap3@) 2.0) )
(sdedr:define-refinement-placement "RefPlace.Cap" "Ref.Cap" "RWin.Cap" )

```

```

(sdedr:define-refinement-window "LWin.Cap" "Rectangle"
  (position (- 0 @Lside@) 0.0 0.0)
  (position -0.175 (- 0 (+ @Hcap1@ @Hcap2@ @Hcap3@)) 0.0) )
(sdedr:define-refinement-size "Ref.Cap1"
  (/ @Ltot@ 2.0) (/ (+ @Hcap1@ @Hcap2@ @Hcap3@) 1.0)
  (/ @Ltot@ 4.0) (/ (+ @Hcap1@ @Hcap2@ @Hcap3@) 2.0) )
(sdedr:define-refinement-placement "RefPlace.Cap1" "Ref.Cap1" "LWin.Cap" )
(sdedr:define-refinement-window "RWin.Spacer" "Rectangle"
  (position 0.0 (+ @Hstop@ @Hba1@ @Hba2@) 0.0)
  (position 0.05 (+ @Hstop@ @Hba1@ @Hba2@ @Hspacer1@ @Hspacer2@)
    0.0) )
(sdedr:define-refinement-size "Ref.Spacer"
  99 (/ (+ @Hspacer1@ @Hspacer2@) 1.0)
  66 (/ (+ @Hspacer1@ @Hspacer2@) 2.0) )
(sdedr:define-refinement-placement "RefPlace.Spacer" "Ref.Spacer" "RWin.Spacer" )
(sdedr:define-refinement-window "LWin.Spacer" "Rectangle"
  (position 0.0 (+ @Hstop@ @Hba1@ @Hba2@) 0.0)
  (position -0.05 (+ @Hstop@ @Hba1@ @Hba2@ @Hspacer1@
    @Hspacer2@) 0.0) )
(sdedr:define-refinement-size "Ref.Spacer1"
  99 (/ (+ @Hspacer1@ @Hspacer2@) 1.0)
  66 (/ (+ @Hspacer1@ @Hspacer2@) 2.0) )
(sdedr:define-refinement-placement "RefPlace.Spacer1" "Ref.Spacer1" "LWin.Spacer"
)

```

.....

```
(sdedr:define-refinement-window "MBWindow.ChannelTop" "Rectangle"
  (position 0.05 (- (+ @Hstop@ @Hba1@ @Hba2@ @Hspacer1@
    @Hspacer2@) 8e-4) 0.0)
  (position 0.075 (- (+ @Hstop@ @Hba1@ @Hba2@ @Hspacer1@
    @Hspacer2@ @Hch@) 0.005) 0.0) )
(sdedr:define-multibox-size "MBSize.ChannelTop"
  99 0.1
  66 8e-4
  1.0 1.5 )
(sdedr:define-multibox-placement "MBPlace.ChannelTop" "MBSize.ChannelTop"
  "MBWindow.ChannelTop" )
(sdedr:define-refinement-window "MBWindow.ChannelTop1" "Rectangle"
  (position -0.05 (- (+ @Hstop@ @Hba1@ @Hba2@ @Hspacer1@
    @Hspacer2@) 8e-4) 0.0)
  (position -0.075 (- (+ @Hstop@ @Hba1@ @Hba2@ @Hspacer1@
    @Hspacer2@ @Hch@) 0.005) 0.0) )
(sdedr:define-multibox-size "MBSize.ChannelTop1"
  99 0.1
  66 8e-4
  1.0 1.5 )
(sdedr:define-multibox-placement "MBPlace.ChannelTop1"
  "MBSize.ChannelTop1" "MBWindow.ChannelTop1" )
```

```

(sdedr:define-refinement-window "MBWindow.ChannelTopT" "Rectangle"
  (position 0.0 (- (+ @Hstop@ @Hba1@ @Hba2@ @Hspacer1@
    @Hspacer2@) 4e-4) 0.0)
  (position 0.05 (- (+ @Hstop@ @Hba1@ @Hba2@ @Hspacer1@
    @Hspacer2@ @Hch@) 0.005) 0.0) )
(sdedr:define-multibox-size "MBSize.ChannelTopT"
  99 0.05
  66 4e-4
  1.0 1.5 )
(sdedr:define-multibox-placement "MBPlace.ChannelTopT" "MBSize.ChannelTopT"
  "MBWindow.ChannelTopT" )
(sdedr:define-refinement-window "MBWindow.ChannelTopT1" "Rectangle"
  (position 0.0 (- (+ @Hstop@ @Hba1@ @Hba2@ @Hspacer1@
    @Hspacer2@) 4e-4) 0.0)
  (position -0.05 (- (+ @Hstop@ @Hba1@ @Hba2@ @Hspacer1@
    @Hspacer2@ @Hch@) 0.005) 0.0) )
(sdedr:define-multibox-size "MBSize.ChannelTopT1"
  99 0.05
  66 4e-4
  1.0 1.5 )
(sdedr:define-multibox-placement "MBPlace.ChannelTopT1"
  "MBSize.ChannelTopT1" "MBWindow.ChannelTopT1" )
(sdedr:define-refinement-window "MBWindow.ChannelBot" "Rectangle"

```

```
(position 0.05 (- (+ @Hstop@ @Hba1@ @Hba2@ @Hspacer1@  
@Hspacer2@ @Hch@) 0.005) 0.0)
```

```
(position 0.075 (+ @Hstop@ @Hba1@ @Hba2@ @Hspacer1@ @Hspacer2@  
@Hch@ 8e-4) 0.0)
```

```
(sdedr:define-multibox-size "MBSize.ChannelBot"
```

```
99 0.1
```

```
66 8e-4
```

```
1.0 -1.5 )
```

```
(sdedr:define-multibox-placement "MBPlace.ChannelBot"
```

```
"MBSize.ChannelBot" "MBWindow.ChannelBot" )
```

```
(sdedr:define-refinement-window "MBWindow.ChannelBot1" "Rectangle"
```

```
(position -0.05 (- (+ @Hstop@ @Hba1@ @Hba2@ @Hspacer1@  
@Hspacer2@ @Hch@) 0.005) 0.0)
```

```
(position -0.075 (+ @Hstop@ @Hba1@ @Hba2@ @Hspacer1@  
@Hspacer2@ @Hch@ 8e-4) 0.0)
```

```
(sdedr:define-multibox-size "MBSize.ChannelBot1"
```

```
99 0.1
```

```
66 8e-4
```

```
1.0 -1.5 )
```

```
(sdedr:define-multibox-placement "MBPlace.ChannelBot1" "MBSize.ChannelBot1"
```

```
"MBWindow.ChannelBot1" )
```

```
(sdedr:define-refinement-window "MBWindow.ChannelBotT" "Rectangle"
```

```
(position 0.0 (- (+ @Hstop@ @Hba1@ @Hba2@ @Hspacer1@ @Hspacer2@  
@Hch@) 0.005) 0.0)
```

```

        (position 0.05 (+ @Hstop@ @Hba1@ @Hba2@ @Hspacer1@ @Hspacer2@
        @Hch@ 4e-4) 0.0) )
(sdedr:define-multibox-size "MBSize.ChannelBotT"
        99 0.05
        66 4e-4
        1.0 -1.5 )
(sdedr:define-multibox-placement "MBPlace.ChannelBotT" "MBSize.ChannelBotT"
"MBWindow.ChannelBotT" )
(sdedr:define-refinement-window "MBWindow.ChannelBotT1" "Rectangle"
        (position 0.0 (- (+ @Hstop@ @Hba1@ @Hba2@ @Hspacer1@ @Hspacer2@
        @Hch@) 0.005) 0.0)
        (position -0.05 (+ @Hstop@ @Hba1@ @Hba2@ @Hspacer1@ @Hspacer2@
        @Hch@ 4e-4) 0.0) )
(sdedr:define-multibox-size "MBSize.ChannelBotT1"
        99 0.05
        66 4e-4
        1.0 -1.5 )
(sdedr:define-multibox-placement "MBPlace.ChannelBotT1"
        "MBSize.ChannelBotT1" "MBWindow.ChannelBotT1" )
(sdedr:define-refinement-window "MBWindow.UnderChannel" "Rectangle"
        (position 0.0 (+ @Hstop@ @Hba1@ @Hba2@ @Hspacer1@ @Hspacer2@
        @Hch@) 0.0)
        (position 0.075 (+ @Hstop@ @Hba1@ @Hba2@ @Hspacer1@ @Hspacer2@
        @Hch@ @Hbu@ @Hsub@) 0.0) )

```

```

(sdedr:define-multibox-size "MBSize.UnderChannel" 99 66
    66 16e-4 1.0 2.0 )
(sdedr:define-multibox-placement
    "MBPlace.UnderChannel"
    "MBSize.UnderChannel" "MBWindow.UnderChannel" )
(sdedr:define-refinement-window "MBWindow.UnderChannel1" "Rectangle"
    (position 0.0 (+ @Hstop@ @Hba1@ @Hba2@ @Hspacer1@ @Hspacer2@
        @Hch@) 0.0)
    (position -0.075 (+ @Hstop@ @Hba1@ @Hba2@ @Hspacer1@
        @Hspacer2@ @Hch@ @Hbu@ @Hsub@) 0.0) )
(sdedr:define-multibox-size "MBSize.UnderChannel1" 99 66 66 16e-4
    1.0 2.0 )
(sdedr:define-multibox-placement
    "MBPlace.UnderChannel1"
    "MBSize.UnderChannel1" "MBWindow.UnderChannel1" )
(sdedr:define-refinement-window "RWin.ActiveArea" "Rectangle"
    (position 0.0 (- 0 0.01) 0.0)
    (position 0.075 (+ @Hstop@ @Hba1@ @Hba2@ @Hspacer1@
        @Hspacer2@ @Hch@ 0.05) 0.0) )
(sdedr:define-refinement-size "Ref.ActiveArea"
    (/ @Lgate@ 4.0) 0.025
    (/ @Lgate@ 5.0) 0.02 )
(sdedr:define-refinement-placement
    "RefPlace.ActiveArea" "Ref.ActiveArea"
    "RWin.ActiveArea" )
(sdedr:define-refinement-window "RWin.ActiveArea1" "Rectangle"
    (position 0.0 (- 0 0.01) 0.0)

```

```

        (position -0.075 (+ @Hstop@ @Hba1@ @Hba2@ @Hspacer1@
        @Hspacer2@ @Hch@ 0.05) 0.0) )
(sdedr:define-refinement-size "Ref.ActiveArea1"
        (/ @Lgate@ 4.0) 0.025 (/ @Lgate@ 5.0) 0.02 )
(sdedr:define-refinement-placement "RefPlace.ActiveArea1"
        "Ref.ActiveArea1" "RWin.ActiveArea1" )
(sdedr:define-refinement-window "RWin.UnderGate"
        "Rectangle"
        (position 0.0 (- (+ @Hstop@ @tins@) 0.001) 0.0)
        (position (+ (/ @Lgate@ 2) 0.04) (+ @Hstop@ @Hba1@ @Hba2@
        @Hspacer1@ @Hspacer2@) 0.0) )
(sdedr:define-refinement-size "Ref.UnderGate"
        99 (/ (- (+ @Hstop@ @Hba1@ @Hba2@ @Hspacer1@ @Hspacer2@) (+
        @Hstop@ @tins@)) 8.0)
        66 (/ (- (+ @Hstop@ @Hba1@ @Hba2@ @Hspacer1@ @Hspacer2@) (+
        @Hstop@ @tins@)) 10.0))
(sdedr:define-refinement-placement "RefPlace.UnderGate" "Ref.UnderGate"
"RWin.UnderGate")
(sdedr:define-refinement-window "RWin.UnderGate1" "Rectangle"
        (position 0.0 (- (+ @Hstop@ @tins@) 0.001) 0.0)
        (position (- 0 (+ (/ @Lgate@ 2) 0.04)) (+ @Hstop@ @Hba1@ @Hba2@
        @Hspacer1@ @Hspacer2@) 0.0) )
(sdedr:define-refinement-size "Ref.UnderGate1"

```

```

99 (/ (- (+ @Hstop@ @Hba1@ @Hba2@ @Hspacer1@ @Hspacer2@) (+
@Hstop@ @tins@)) 8.0)

66 (/ (- (+ @Hstop@ @Hba1@ @Hba2@ @Hspacer1@ @Hspacer2@) (+
@Hstop@ @tins@)) 10.0))

(sdedr:define-refinement-placement "RefPlace.UnderGate1"
"Ref.UnderGate1" "RWin.UnderGate1")

(sdedr:define-refinement-window "MBWindow.SchottkyGate" "Rectangle"
(position 0.0 (+ @Hstop@ @tins@) 0.0)
(position (+ (/ @Lgate@ 2) 0.04) (+ (+ @Hstop@ @tins@) 0.01) 0.0))

(sdedr:define-multibox-size "MBSize.SchottkyGate"
(/ @Lgate@ 10.0) 0.05 (/ @Lgate@ 12.0) 4e-4 1.0 1.5 )

(sdedr:define-multibox-placement "MBPlace.SchottkyGate"
"MBSize.SchottkyGate" "MBWindow.SchottkyGate" )

(sdedr:define-refinement-window "MBWindow.SchottkyGate1" "Rectangle"
(position 0.0 (+ @Hstop@ @tins@) 0.0)
(position (- 0 (+ (/ @Lgate@ 2) 0.04)) (+ (+ @Hstop@ @tins@) 0.01) 0.0))

(sdedr:define-multibox-size "MBSize.SchottkyGate1"
(/ @Lgate@ 10.0) 0.05 (/ @Lgate@ 12.0) 4e-4 1.0 1.5 )

(sdedr:define-multibox-placement "MBPlace.SchottkyGate1"
"MBSize.SchottkyGate1" "MBWindow.SchottkyGate1" )

(sde:set-meshing-command "snmesh")

(sde:build-mesh "snmesh" "-a -c boxmethod" "n@node@")

(system:command "svisual sdemodel_msh.tdr &")

```

Appendix B

THE SDEVICE CODES

Appendix B shows the contact definition, applied physic models, plot information, and the calculation methods.

Electrode{

```
{ Name="s" Voltage= 0.0 Resistor= 100 }  
{ Name="d" Voltage= 0.0 Resistor= 100 }  
{ Name="g" Voltage= 0.0 Schottky Barrier= 0.83  
  eRecVelocity= 1.e7 hRecVelocity= 1.e7 }  
{ Name="b" Voltage= 0.0 Resistor= 1e3 } }
```

File{

```
Grid= "n@previous@_msh.tdr"  
Current= "@plot@"  
Output= "@log@"  
Plot= "@tdrdat@"  
Parameter= "models.par" }
```

Physics {

```
Areafactor=1  
Hydrodynamic( eTemperature )  
Fermi  
Mobility(  
eHighFieldSaturation(CaugheyThomas CarrierTempDrive))  
EffectiveIntrinsicDensity( NoBandGapNarrowing )  
Recombination(SRH Auger Radiative)}
```

```

Physics( Region="substrate"){
Traps((Donor Conc=1e16 EnergyMid=0.61 fromCondBand
exsection=2.5e-18 hXsection=2.5e-16))}
Physics( Region="cap1"){
MoleFraction(xFraction=0.48)}
Physics( Region="cap1_t18"){
MoleFraction(xFraction=0.48)}
Physics( Region="cap2"){
MoleFraction(xFraction=0.47)}
Physics( Region="cap2_t20"){
MoleFraction(xFraction=0.47)}
Physics( Region="cap3"){
MoleFraction(xFraction=0.3)}
Physics( Region="cap3_t22"){
MoleFraction(xFraction=0.3)}
Physics( Region="barrier1"){
MoleFraction(xFraction=0.48)}
Physics( Region="barrier1_t4"){
    MoleFraction(xFraction=0.48)}
Physics( Region="barrier2"){MoleFraction(xFraction=0.48)}
Physics( Region="spacer1"){MoleFraction(xFraction=0.48)}
Traps((Donor Conc=1e16 EnergyMid=0.61 fromCondBand
exsection=2.5e-18 hXsection=2.5e-16))}
Physics( Region="buffer"){

```

```
MoleFraction(xFraction=0.48)}
```

```
Physics( Region="spacer2"){
```

```
MoleFraction(xFraction=0.3)}
```

```
Physics( Region="channel"){
```

```
MoleFraction(xFraction=0.3)}
```

```
Plot{
```

```
*--Density and Currents, etc
```

```
  eDensity hDensity
```

```
  TotalCurrent/Vector eCurrent/Vector hCurrent/Vector
```

```
  eMobility hMobility
```

```
  eVelocity hVelocity
```

```
  eQuasiFermi hQuasiFermi
```

```
*--Temperature
```

```
  eTemperature
```

```
  * hTemperature Temperature
```

```
*--Fields and charges
```

```
  ElectricField/Vector Potential SpaceCharge
```

```
*--Doping Profiles
```

```
  Doping DonorConcentration AcceptorConcentration
```

```
*--Generation/Recombination
```

```
  SRH Auger
```

```
  AvalancheGeneration eAvalancheGeneration hAvalancheGeneration
```

```
*--Driving forces
```

```
  eGradQuasiFermi/Vector hGradQuasiFermi/Vector
```

```

    eParallel hParallel
*--Band structure/Composition
    BandGap
    * BandGapNarrowing
    Affinity
    ConductionBand ValenceBand
    xMoleFraction
*--Traps
    eTrappedCharge hTrappedCharge
    eGapStatesRecombination hGapStatesRecombination
*--Heat generation
    * TotalHeat eJouleHeat hJouleHeat RecombinationHeat }

```

Math{

```

    Extrapolate
    Digits= 5
    Notdamped= 50
    Iterations= 50
    RelErrControl
    ErrRef(Electron) = 1e7
    ErrRef(Hole) = 1e7
    RelTermMinDensity= 1e4
    RelTermMinDensityZero= 1e7
}

```

```

Solve {
  *- Build-up of initial solution:
  NewCurrentFile="init"
  Coupled(Iterations= 100){ Poisson }
  Coupled{ Poisson Electron Hole }
  Coupled{ Poisson Electron Hole eTemperature }
  *--eTemperature
  *- Bias gate to target bias
  Quasistationary(
    InitialStep=1e-6 Increment=1.1
    MinStep=1e-15 MaxStep=0.0005
    Goal{ Name="g" Voltage= @Vgmax@ }
  ){ Coupled{ Poisson Electron Hole eTemperature } }
  *- drain voltage sweep
  NewCurrentFile="IdVd"
  Quasistationary(
    InitialStep=1e-6 Increment=1.1
    MinStep=1e-15 MaxStep=0.005
    Goal{ Name="d" Voltage= @Vd@ }
  ){ Coupled{ Poisson Electron Hole eTemperature }
    CurrentPlot(Time=(Range=(0 1) Intervals=100))}

```